The Evolution and Stability of Finite-Amplitude Mountain Waves. Part II: Surface Wave Drag and Severe Downslope Windstorms

W. R. PELTIER[1]

Advanced Studies Program, National Center for Atmospheric Research, Boulder, CO 80307

T. L. CLARK

National Center for Atmospheric Research, Boulder, CO 80307

(Manuscript received 3 October 1978, in final form 29 March 1979)

ABSTRACT

The transient evolution of internal waves which are forced by the flow of stably stratified fluid over two-dimensional topography exhibits several pronounced nonlinear effects for geophysically relevant values of the governing parameters. For homogeneous flows in which the internal Froude number is constant, the importance of nonlinearity is determined by the aspect ratio of the topography and the flow in the steady-state regime is as predicted by Long's model. When the background flow is inhomogeneous, Long's model no longer applies and new nonlinear effects may occur. One example of such an effect is the marked increase in the efficiency with which resonant lee waves are excited beyond the linear efficiency. A second example concerns the possibility of the trapping and subsequent amplification of the internal wave beneath its own level of supercritical steepening. The latter process appears to be important in understanding the strong downslope windstorm which occurred at Boulder, Colorado, on 11 January 1972.

1. Introduction

In a recent article (Clark and Peltier, 1977; hereafter called I) we described an initial investigation of the temporal evolution of internal waves forced by finite aspect ratio topography. Our analysis was restricted to consideration of homogeneous background flows and the purpose of the present article is to extend the work to encompass inhomogeneous models in which the characteristics of the nonlinear development may be complex. We shall also reconsider our earlier time-dependent solutions to the homogeneous problem in the light of Long's model.

We showed in I, by direct numerical simulation, that the freely propagating disturbance initiated by stratified flow over an isolated obstacle exhibited a rather sharp transition in the nature of its temporal development when the aspect ratio of the topography $A = h/a$ (h = height; a = halfwidth) exceeded a critical value A_c. The numerical evidence for this transition was obtained by analysis of the evolution of forced waves in a homogeneous flow with constant Brunt-Väisälä frequency and uniform horizontal wind. The solution of this simple nonlinear initial value problem is entirely determined by two nondimensional parameters if the Reynolds number is infinite. These parameters are the aspect ratio A and the Froude number $\mathrm{Fr} = a^2N^2/U^2$ (N = Brunt-Väisälä frequency; U = background wind speed) which determines whether the forced disturbance will be freely propagating or evanescent. For $\mathrm{Fr} > O(1)$ the response is in the internal wave regime and it is in this regime that the sharp transition was found. With $\mathrm{Fr} > 1$ and $A > A_c$, the wave drag on the surface was found to amplify continuously (and linearly) in time, eventually obtaining values which exceeded the linear prediction for the same parameters by several *hundred* percent. The critical aspect ratio beyond which the apparent instability was realized was found to agree well with an *a posteriori* prediction based upon linear steady-state theory, at least for the single flow investigated in I (for which the critical aspect ratio was small).

For fixed Fr, A_c is the aspect ratio such that there exists a streamline within the first vertical wavelength of the standing wave structure which locally achieves a vertical orientation. If this critical condition is exceeded, it is normally associated with the formation of "rotors" in the region of reversed streamlines (e.g., Miles, 1969; Long, 1972), the flow in this vicinity being locally unstable against convection. The "breaking" of the internal wave is synonymous with the release of this local secondary instability. That this critical aspect ratio should also mark an abrupt transition in the flow from states

[1] Alfred P. Sloan Foundation Fellow. Permanent affiliation: Department of Physics, University of Toronto, Toronto, Ontario, Canada M5S-1A7.

0022-4928/79/081498-32$12.00

($A < A_c$) in which the surface drag is close to that predicted by linear theory to new states ($A > A_c$) in which the surface drag is very much in excess of the linear prediction, is not immediately obvious.

The first idea we wish to explore in the present paper concerns this apparent connection between states of high surface drag and states in which supercritical steepening of the streamlines occurs. This connection, which is most readily seen in terms of Long's model, is extremely important to the phenomenon of strong downslope windstorms. In the high-drag state, the strength of the downslope flow in the lee of the mountain is very much stronger than would be predicted by linear theory. Nonlinearity may therefore be very important to the mechanics of the windstorm phenomenon to the extent that it completely dominates other effects.

In the theory of downslope windstorms recently advanced by Klemp and Lilly (1975), the mechanics of the phenomenon are basically linear. They suggest that a strong surface response occurs whenever the mean vertical wavelength of the disturbance is such that the distance between the ground and the tropopause is an integral number of half-wavelengths (see also Blumen, 1970; Blumen and McGregor, 1976). Under such conditions there is constructive interference between the direct wave from the surface and the partial reflection from the tropopause and a modest increase in the surface response. In their view, then, the occurrence of a windstorm demands a rather special tuning of the mean flow parameters [essentially $N(z)$, $U(z)$ since they assume $\mathrm{Fr} \gg 1$ and use completely hydrostatic models to describe the wave field].

Our preliminary nonlinear results in I demonstrating the sharpness of the transition from the regime in which linear theory is valid to that in which the nonlinearity of the lower boundary condition is very important, were clouded to a certain extent for several reasons. First, in the supercritical regime where the disturbance is amplifying, we introduced locally enhanced diffusivity for both heat and momentum in the vicinity of the wave-induced critical "level" (remember that the high-drag state is characterized by supercritically steepened streamlines; because the region of reversed streamlines is also a region of reversal of the local wind direction we shall refer to it as a critical "level" in the flow). This was done in an attempt to parameterize the effect of small-scale convection which we assumed to be associated with the locally superadiabatic temperature gradient. A simple first-order closure scheme (Smagorinski, 1963; Lilly, 1962) was employed to estimate the turbulence intensity. It might be argued that the strong amplification for $A > A_c$ was a consequence of the turbulence parameterization, the physical basis of which is questionable. Second, we did not show explicit comparisons of the effect of resolution on the solutions nor did we illustrate that the results were insensitive to the location of the lateral boundaries with respect to the domain interior. Rather, we simply stated that the required calculations had been performed and that the results were negative (i.e., the solutions were insensitive to such variations). A further and equally important question which one might legitimately raise concerns the relevance of this strong nonlinearity to actual atmospheric flows which are quite unlike the simple homogeneous flows discussed in I.

In the present paper we have attempted to resolve each of these issues in turn and to explore in detail the various other sources of nonlinearity which may obtain in nonhomogeneous flows. All of these effects contribute to the determination of the intensity of the wind speed to the lee of the topographic maximum. In Section 2 a simple, linear, inhomogeneous steady-state model is described which we have used for control on the full nonlinear time-dependent calculations. In Section 3 we provide a summary description of the nonlinear, nonhydrostatic, numerical model for completeness. However, since most of the description has been published elsewhere (Clark, 1977; Clark and Peltier, 1977) the discussion is brief and confined to a statement of the basic equations and of the alterations of the model which were necessary for the present calculations.

In Section 4 we will discuss the nonlinear effects which occur in homogeneous flows through a more detailed analysis of that considered in I. We will compare the time-dependent numerical solutions in the long time limit both to the prediction of linear steady-state theory and to the results expected from Long's model. The reason for the rather sharp transition between the low-drag and high-drag states for $A \gtrless A_c$ will be discussed in detail.

In Section 5 we consider the response of a model atmosphere in which the vertical variations of wind speed and stability are those appropriate to "standard" midlatitude winter conditions. We use the linear inhomogeneous model to obtain an upper bound on the critical aspect ratio and show thereby that the high-drag regime should be typical of the topography associated with the Canadian and U.S. Rocky Mountains. We then use the nonlinear time-dependent model to calculate the evolution of the wave field for both $A \gtrless A_c$. For $A > A_c$ the nonlinear increase of the wave drag and the associated increase in the downslope wind speed are the same as in the homogeneous model.

In Section 6 we describe the evolution of the wave field in a third model atmosphere which differs from the standard winter case mainly in that the jet is more intense. When it is subject to the same bell-shaped forcing, this atmosphere supports a strong linear resonant "lee wave." Such trapped disturbances are

a common atmospheric occurrence and are responsible for the regularly spaced cloud bands which are often seen in satellite photographs to lie parallel to the ridge downstream of the topography. Since such disturbances are intrinsically nonhydrostatic and since their nonlinear time-dependent description places severe strains on a finite-difference model, we will use our simulation of them as further evidence of the fidelity of the model. Such modes have not previously been simulated numerically in a model which has a nonreflecting upper boundary condition. The effect of nonlinearity upon the efficiency with which they are generated turns out to be extremely important and in the sense of strongly increasing the lee wave amplitude above that which would be predicted by linear theory.

In Section 7 we compare the predictions of the nonlinear time-dependent model with observations of the 11 January 1972 severe windstorm in Boulder, Colorado, described by Lilly and Zipser (1972). The observed upstream conditions during this storm differ from those employed for the lee wave simulation only in that the stratospheric wind speed has a magnitude of 20 m s^{-1} in accord with the observations rather than 30 m s^{-1}. With this modification of the background wind speed in the upper levels, the solution undergoes a drastic change of character since the internal wave now breaks in the lower stratosphere. Subsequent to wave breaking the tropospheric flow develops strongly and the final deflection of the tropopause is such that it exceeds the mountain height by approximately a factor of 3. We comment upon the nature of the nonlinearity which supports the accompanying dramatic development of the downslope windstorm.

In conclusion, in Section 8 we summarize the main results which have been obtained to date and we briefly discuss their implications to the problem of parameterizing the effect of mountain wave drag in atmospheric general circulation models (Lilly, 1972).

2. A linear, inhomogeneous, steady-state model

This model will be employed for control on the nonlinear time-dependent calculations to be described in later sections. It is the simplest linear steady-state model which is capable of accurately describing the structure of mountain wave disturbances in an inhomogeneous flow and employs what have come to be called "multiple-layer" methods. The background state of the atmosphere is approximated by a stack of layers in each of which the wind speed and temperature are constant. It is well known that this approximation is adequate to the extent that the local vertical wavelength is everywhere much greater than the layer thickness. Since this method is reasonably well known (e.g., Hines and Reddy, 1967) we will describe our implementation of it as briefly as possible and will forego derivation of the linearized field equations upon which it is based since these are equally well established.

In the mth layer the horizontal wavenumber domain form of the steady-state solution for the perturbation ψ' of the variable ψ has the form

$$\psi'_m \propto \exp[ikx + s_m \pm ik_{z,m}(z - z_{m-1})], \quad (1)$$

where $s_m = \frac{1}{2}H_m$ and H_m is the isothermal scale height in the mth layer. The quantity z_m is the height z to the *top* of the mth layer in the absence of a wave and $k_{z,m}$ is the vertical wavenumber of the wave in layer m which is determined by the dispersion relation

$$k_{z,m}^2 = \left(\frac{\omega_{g,m}^2}{\Omega_m^2} - 1\right)k^2 + \frac{\Omega_m^2 - \omega_{A,m}^2}{c_m^2}. \quad (2)$$

In Eq. (2) $\omega_{g,m}$ is the isothermal Brunt-Väisälä frequency in layer m, $\Omega_m = kU_m$ is the intrinsic frequency of the wave, $\omega_{A,m} = g\gamma/2c_m$ is the acoustic cutoff frequency and c_m is the sound speed. If $\tilde{w}_m$ is the complex amplitude of the vertical velocity perturbation in k-space, then the following polarization relations connect the Fourier amplitudes of the other variables to it:

$$\tilde{p}_m^{\pm} = \frac{\Omega_m[\pm\gamma k_{z,m} - i(1 - \gamma/2)/H_m]}{\Omega_m^2 - k^2c_m^2}\tilde{w}_m^{\pm}, \quad (3a)$$

$$\tilde{\rho}_m^{\pm} = \frac{\Omega_m^2(\mp k_{z,m} - i/H_m) + i(\gamma - 1)gk^2}{\Omega_m(\Omega_m^2 - k^2c_m^2)}\tilde{w}_m^{\pm}, \quad (3b)$$

$$\tilde{u}_m^{\pm} = -(kc_m^2/\gamma\Omega_m)\tilde{p}_m^{\pm}, \quad (3c)$$

where $\tilde{p}_m$, $\tilde{\rho}_m$ and $\tilde{u}_m$ respectively describe the perturbation pressure, density and horizontal velocity amplitudes in the mth layer and in the horizontal wavenumber domain. The upper and lower signs in (3) correspond to the upper and lower signs in (1) and thus denote the upward and downward propagating waves in each layer of the stack. On each of the interior layer boundaries we require continuity of the displacement so that $\tilde{w}/\Omega$ must be continuous across all such interfaces. This kinematic condition must be supplemented by the dynamic requirement for continuity of the normal stress across the perturbed interface. This leads (e.g., see Hines and Reddy, 1967) to the demand that the quantity $\tilde{\chi} = (\partial\tilde{u}/\partial x + \partial\tilde{w}/\partial z)\Omega^{-1}$ be continuous across the unperturbed interface. If A_m and B_m are the amplitudes of the upgoing and downgoing waves in the mth layer, i.e.,

$$\tilde{w}_m = \tilde{w}_m^+ + \tilde{w}_m^- = e^{s_m(z-z_{m-1})}[A_m e^{ik_{z,m}(z-z_{m-1})} + B_m e^{ik_{z,m}(z-z_{m-1})}]e^{ikx}, \quad (4)$$

then application of the two interfacial boundary conditions leads to a so-called transmission matrix

relation connecting the coefficients A_{m+1}, B_{m+1} to A_m, B_m. The explicit form of this relation is

$$\begin{bmatrix} A_{m+1} \\ B_{m+1} \end{bmatrix} = \frac{h_m \Omega_{m+1}}{2i\Omega_m M_{m+1}} [E_m] \begin{bmatrix} A_m \\ B_m \end{bmatrix}, \quad (5)$$

where the transmission matrix E_m is

$$[E_m] = \begin{bmatrix} (\epsilon_{1,1})_m & (\epsilon_{1,2})_m \\ (\epsilon_{2,1})_m & (\epsilon_{2,2})_m \end{bmatrix}, \quad (6)$$

the individual elements of which are

$$\left.\begin{aligned} (\epsilon_{1,1})_m &= Q_{m+1} e^{ik_{z,m}d_m} - P_m e^{ik_{z,m}d_m} \\ (\epsilon_{1,2})_m &= Q_{m+1} e^{-ik_{z,m}d_m} - Q_m e^{-ik_{z,m}d_m} \\ (\epsilon_{2,1})_m &= P_{m+1} e^{ik_{z,m}d_m} + P_m e^{ik_{z,m}d_m} \\ (\epsilon_{2,2})_m &= -P_{m+1} e^{-ik_{z,m}d_m} + Q_m e^{-ik_{z,m}d_m} \end{aligned}\right\}. \quad (7)$$

In Eqs. (5)–(7) we have used the following definitions: $h_m = \exp(s_m d_m)$, $d_m = z_m - z_{m-1}$, $M = k_z\Omega^2/(k^2c^2 - \Omega^2)$, $N = (k^2g - s\Omega^2)/(k^2c^2 - \Omega^2)$, $P = N - iM$, $Q = P^*$. From (5) it therefore follows that the coefficients in layer $m + 1$ are related to those in layer $r (r \leq m)$ by

$$\begin{bmatrix} A_{m+1} \\ B_{m+1} \end{bmatrix} = f_r^m [\Delta_r^m] \begin{bmatrix} A_r \\ B_r \end{bmatrix}, \quad (8)$$

where

$$f_r^m = \prod_{j=r}^{m} \frac{h_j \Omega_{j+1}}{2i\Omega_j M_{j+1}} \quad (9)$$

and the "propagator matrix" Δ_r^m is

$$[\Delta_r^m] = \begin{bmatrix} (\delta_{1,1})_r^m & (\delta_{1,2})_r^m \\ (\delta_{2,1})_r^m & (\delta_{2,2})_r^m \end{bmatrix} = [E_m] \cdot [E_{m-1}] \cdots [E_r]. \quad (10)$$

To complete the solution we have yet to specify the upper and lower boundary conditions. The kinematic condition at the lower boundary requires

$$\tilde{w}_1(z = 0) = A_1 + B_1 = ikU_1 z(k), \quad (11)$$

where $z(k)$ is the wavenumber spectrum of the surface topography $z(x)$, and U_1 is the background velocity in the lowest layer near the surface. The topmost layer in the stack is a half-space in which the background wind and temperature are assumed to be constant. In this region the perturbation energy flux must be outgoing, i.e., the Sommerfeld condition applies. If we call the upper half-space region n then this requires $B_n = 0$ and from (8) with $r = 1$ we obtain the following relation between A_n and (A_1, B_1):

$$\begin{bmatrix} A_n \\ 0 \end{bmatrix} = f_1^{n-1} \begin{bmatrix} (\delta_{1,1})_1^{n-1} & (\delta_{1,2})_1^{n-1} \\ (\delta_{2,1})_1^{n-1} & (\delta_{2,2})_1^{n-1} \end{bmatrix} \begin{bmatrix} A_1 \\ B_1 \end{bmatrix}, \quad (12)$$

so that in addition to (11) we have the second constraint on (A_1, B_1) that

$$(\delta_{2,1})_1^{n-1} A_1 + (\delta_{2,2})_1^{n-1} B_1 = 0. \quad (13)$$

Combining (11) and (13) we obtain the following explicit expressions for A_1 and B_1:

$$A_1 = \frac{-(\delta_{2,2})_1^{n-1}}{(\delta_{2,1})_1^{n-1} - (\delta_{2,2})_1^{n-1}} \tilde{w}_1(z = 0), \quad (14a)$$

$$B_1 = \frac{(\delta_{2,1})_1^{n-1}}{(\delta_{2,1})_1^{n-1} - (\delta_{2,2})_1^{n-1}} \tilde{w}_1(z = 0). \quad (14b)$$

With A_1 and B_1 now determined we obtain the $\tilde{w}$ field everywhere by substituting (8) into (4). Given $\tilde{w}(k,z)$ determined in this fashion we may deduce the field $\tilde{w}(x,z)$ by evaluation of the Fourier inversion integral.

It is more useful for our present purposes, however, to express the solution in terms of the "free stream deflection" $\xi(x,z)$ as in I. Since by definition $w(x,z) = d\xi(x,z)/dt$, we then have $\tilde{w}(k,z) = ikU(z)\tilde{\xi}(k,z)$ to first order in deviations from the background hydrostatic equilibrium configuration. The complete solution for the ξ field in layer m is thus

$$\xi_m(x,z) = \mathrm{Re}\left[\pi^{-1} e^{s_m(z - z_{m-1})} \int_0^\infty \frac{A_m e^{ik_{z,m}(z - z_{m-1})} + B_m e^{-ik_{z,m}(z - z_{m-1})}}{ikU_m} e^{ikx} dk \right], \quad (15)$$

where Re indicates "the real part of". This may be rewritten in the conventional form

$$\xi(x,z) = \mathrm{Re}\left[\int_0^\infty C(k) \frac{f(k,z)}{f(k,0)} e^{ikx} dk \right], \quad (16)$$

where the secular function $f(k,0)$ is just

$$f(k,0) = (\delta_{2,1})_1^{n-1} - (\delta_{2,2})_1^{n-1}. \quad (17)$$

The zeros of the secular function are poles of the integrand in (16) when this is considered as a function of complex k. Poles which lie just off the real k axis are extremely important in the mountain wave problem since these "leaky modes" are intimately related to the so-called lee waves about which we shall have more to say in later sections. Poles which lie on the real axis may be treated analytically (e.g., as in Vergeiner, 1971) although such singularities are not important in any of the model calculations which we shall describe here. Poles which lie just off the real axis contribute sharp resonant lines to the spectrum of the solution [e.g., the integrand of Eq. (16)] but these present no difficulty if the spectrum is sampled at sufficiently small Δk and the integral (16) may be

evaluated by direct FFT since the spectrum is band-limited. Given $\xi(x,z)$ for the steady-state response determined in this fashion, there are several characterizations of the solution which we will require in later sections and these are listed for convenience as follows:

a. The mass flux streamfunction $\phi(x,z)$

This function is defined such that $\rho_0 u = \partial\phi/\partial z$ and $\rho_0 w = -\partial\phi/\partial x$, where $u(x,z)$ and $w(x,z)$ are the *total* horizontal and vertical components of velocity, respectively. Using $w = U(z)(\partial\xi(x,z)/\partial x)$, then on the assumption of no upstream influence we have

$$\phi(x,z) = -\xi(x,z)\rho_0(z)U(z) + \int_0^z U(z')\rho_0(z')dz'. \quad (18)$$

b. Horizontal wind perturbation $u' = u - U$

This parameter may be obtained by direct integration of the anelastic form of the continuity equation under the assumption of no upstream influence. The result is

$$u'(x,z) = U\left(-\frac{\partial\xi}{\partial z} - \frac{\xi}{U}\frac{\partial U}{\partial z} - \frac{\xi}{\rho_0}\frac{\partial\rho_0}{\partial z}\right). \quad (19)$$

c. The downslope wind amplification factor M

This function provides a useful nondimensional linear measure of the windstorm potential of a given combination of mean flow and topography. It is simply (19) evaluated on the surface $z = 0$ and normalized with respect to the surface wind speed, i.e.,

$$M(x) = \frac{u'(x,0)}{U(0)} = \left(-\frac{\partial\xi}{\partial z} - \frac{\xi}{U}\frac{\partial U}{\partial z} - \frac{\xi}{\rho_0}\frac{\partial\rho_0}{\partial z}\right)_{z=0}. \quad (20)$$

d. Stability indices I_1 and I_2

These functions are critical to the analysis which concerns us in the present paper. They provide two alternative linear *a posteriori* estimates of the aspect ratio A_c above which the mountain wave should become unstable in some sense. For adiabatic flow the two indices predict *exactly* the same A_c. Under such conditions $d\theta/dt = 0$, where θ is the potential temperature, and the steady-state linearized form of this expression of the second law reduces to (with $w = U\partial\xi/\partial x$)

$$\frac{\partial\theta'}{\partial x} + \frac{\partial\xi}{\partial x}\frac{\partial\theta_0}{\partial z} = 0, \quad (21)$$

where $\theta_0(z)$ is the background potential temperature field and $\theta'(x,z)$ the deviation from it. Eq. (21) may be integrated once assuming no upstream influence to give $\theta'(x,z) = -\xi(x,z)\partial\theta_0/\partial z$ and this may be differentiated with respect to z to give

$$\frac{\partial\theta'(x,z)}{\partial z} = -\frac{\partial\theta_0}{\partial z}\frac{\partial\xi}{\partial z} - \frac{\partial^2\theta_0}{\partial z^2}\xi(x,z). \quad (22)$$

Now locally the static stability of the free stream will be completely eroded by the wave where $-\partial\theta'/\partial z > \partial\theta_0/\partial z$ and a local region of *static* instability will be created. Therefore, defining

$$I_1(x,z) = \frac{\partial\xi}{\partial z} + \frac{\xi(x,z)\dfrac{\partial^2\theta_0}{\partial z^2}}{\dfrac{\partial\theta_0}{\partial z}}, \quad (23)$$

in linear *a posteriori* condition for local convective instability is

$$\{I_1(x,z)\}_{\max} > 1, \quad (24)$$

which reduces to the condition employed in paper I when the curvature of the $\theta_0(z)$ profile vanishes as is the case for uniform stratification. Since ξ scales linearly with the mountain height with all other parameters fixed we may predict the critical mountain height for which a region of instability will be induced on the basis of a single calculation of $\xi(x,z)$ as discussed in I.

An alternative to the stability index I_1, which predicts the same critical aspect ratio, follows from the fact that for adiabatic frictionless flow the isentropes are also streamlines. This is perhaps obvious but can be seen directly by expanding the steady-state adiabatic condition as $u\partial\theta/\partial x + w\partial\theta/\partial z = 0$, where $u = u' + U$, $\theta = \theta' + \theta_0$, $w = w'$. Substituting for u and w in terms of the total streamfunction we then obtain $J(\theta,\phi) = 0$, where J is the Jacobian operator. Thus, ϕ and θ are linearly dependent and where $I_1(x,z) = 1$ the streamlines are vertical since $\partial\phi/\partial z = \partial(\theta_0 + \theta')/\partial z = 0$. Where this condition is satisfied the horizontal wind vanishes. From (19) the condition for the horizontal wind to vanish is just

$$I_2(x,z) = \frac{u}{U} = 1 - \frac{\partial\xi}{\partial z} - \frac{\xi}{U}\frac{\partial U}{\partial z} - \frac{\xi}{\rho_0}\frac{\partial\rho_0}{\partial z} = 0 \quad (25)$$

and thus a second measure of instability to that provided by I_1 is

$$\{I_2(x,z)\}_{\min} < 0. \quad (26)$$

In fact (26) is preferable to (24) since it does not involve the curvature of the basic state profiles and so may be calculated to higher accuracy. This is particularly convenient when the basic state is known only at a discrete set of sampling points and values of the parameters elsewhere must be determined by interpolation.

The main point to note from the above discussion is that in the steady-state mountain wave problem, the region in which the background static stability is erased by the wave is also the region of reversed streamlines. In its supercritical state the wave induces its own critical level and we call this region a *nonlinear critical level* to emphasize the fact that it exists in consequence of the existence of the wave. The main question which concerns us here is what happens to the mountain wave in the course of its *transient* evolution as the critical region is established while the disturbance propagates upward from the lower boundary? Important quantities in the analysis of the effects which occur are the height z_c above the surface at which the critical region forms and the wave drag $D_w(0)$ on the surface itself.

e. The height z_c of the wave-induced critical level

Suppose we consider a bell-shaped topography as in I with $z_s(x) = a^2h/(x^2 + a^2)$, where h is the mountain height and a its halfwidth. For a homogeneous flow with constant background wind and stability the solution for the free-stream deflection $\xi(x,z)$ is just

$$\xi(x,z) = \mathrm{Re}\left[ahe^{z/2H}\int_0^\infty dk \times \exp\{-ak + i[kx + (k_G^2 - k^2)^{1/2}z]\}\right]. \quad (27)$$

To the extent that the disturbance is hydrostatic then the long-wave limit $k_G^2 = N^2/U^2 \gg k^2$ applies and (27) may be evaluated as in Miles and Huppert (1969) using Hilbert transforms. The result is

$$\xi^L(x,z) = \frac{a^2h}{x^2 + a^2} e^{z/2H}\cos k_G z - \frac{ahx}{(x^2 + a^2)} e^{z/2H}\sin k_G z, \quad (28)$$

where $\xi^L(x,z)$ is the longwavelength approximation to (27). Now the condition for instability of this wave is just $\partial\xi/\partial z > 1$ and since (assuming $H \gg z$)

$$\frac{\partial\xi^L}{\partial z} \approx \frac{-a^2h}{x^2 + z^2} k_G e^{z/2H}\sin k_G z - \frac{ahx}{(x^2 + a^2)} k_G e^{z/2H}\cos k_G z, \quad (29)$$

we see that the local extrema of $\partial\xi^L/\partial z$ are all found immediately overhead of the mountain ($x = 0$) and that the first steepening level occurs where $k_G z_c = 3\pi/2$ which is the first maximum of (29) above the surface $z = 0$. The wave-induced critical level is therefore located at a height $3\lambda_z/4$ above the surface (where $\lambda_z = 2\pi/k_G$ is the vertical wavelength of the wave) and this point is located directly overhead of the topographic maximum when the disturbance is linear and hydrostatic. For an inhomogeneous flow in which the basic wave is still strongly hydrostatic we may generalize this result in the WKB limit to obtain

$$\int_0^{z_c} k_z(z')dz' = 3\pi/2 \quad (30)$$

which just states that the point at which the wave is first expected to break is located at a height z_c such that the integrated phase shift between it and the ground is $3\pi/2$. Eq. (30) has provided a good estimate of z_c for all of the flows which we shall investigate here, even for those in which the nonlinearity is extreme.

f. The surface wave drag $D_w(0)$

Associated with the steady-state wave field (15) there is a downstream pressure drop across the topography and thus a force on the earth. This force (per unit length of the topography) is just

$$D_w(z = 0) = -\rho_0 \int_{-\infty}^{+\infty} u'w'dx \quad (31)$$

which is just the negative of the Reynolds stress evaluated on the surface $z = 0$. The Eliassen-Palm (1960) theorem assures us that so long as the wave amplitude is small the Reynolds stress in the interior will be nondivergent. Thus if the wave has small amplitude, the mean flow will not be affected by its transmission. Our interest here is in circumstances in which the wave amplitude is not small and thus we are explicitly concerned with processes that occur when the Eliassen-Palm theorem is violated.

The linear model described above has proven to be very useful in understanding the results obtained from our nonlinear simulations and as a relatively inexpensive tool for designing the experiments themselves. It will be employed extensively in later sections. We have tested this numerical model by reproducing the results of the analytic solution obtained in I for the homogeneous atmosphere. The $\xi(x,z)$ and $w(x,z)$ fields are shown in Figs. 1 and 2, respectively, for this model for which the parameters are $U = 4$ m s^{-1}, $2\pi/\omega_g = 10.3$ min, $a = 3$ km, $h = 100$ m. $\xi(x,z)$ is deduced by the FFT of the discretized spectrum as in (16), and $w(x,z)$ is deduced using centered finite differences on the ξ field as in I. The surface drag was calculated by evaluating the correlation (31) using quadrature rather than the exact formula in I and found to be 302.5 kg s^{-2} which is within 1% of the previous calculation with surface density $\rho_0 = 1.276$

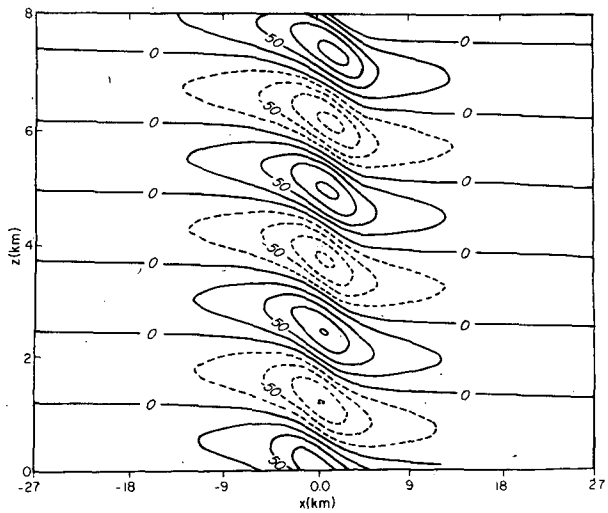

FIG. 1. Contours of constant (steady-state) free-stream deflection $\xi(x,z)$ based on linear inviscid theory. The dashed contours are for ξ negative and the solid for ξ positive. The parameters are $2\pi/N = 10.2$ min, $U = 4$ m s^{-1}, $a = 3$ km, $h = 100$ m.

kg m^{-3}. Using either of the criteria (24) or (26) for stability we again find that the critical mountain height beyond which the flow becomes unstable is $h_c = 400$ m so that the critical aspect ratio is $A_c \approx {}^2/_{15}$ as previously.

Before proceeding with a discussion of the nonlinear time-dependent experiments we provide a summary description in the next section of the properties of the finite-difference model.

3. The nonlinear time-dependent model

The numerical model employed in the calculations discussed in the following sections is based on that described in detail in Clark (1977) and Clark and Peltier (1977). The term $\partial\rho/\partial t$ is dropped from the continuity equation and the resulting anelastic system therefore does not support sound waves. The equations of momentum conservation, continuity and internal energy conservation then become, respectively,

$$\bar{\rho}\frac{d\mathbf{u}}{dt} = -\nabla p' + \rho'\mathbf{g} + \nabla\cdot\boldsymbol{\tau}, \tag{32a}$$

$$\nabla\cdot(\bar{\rho}\mathbf{u}) = 0, \tag{32b}$$

$$\bar{\rho}\frac{d\theta}{dt} = \nabla\cdot\mathbf{H}, \tag{32c}$$

where $\boldsymbol{\tau}$ is the stress tensor, $\mathbf{H}$ the heat flux vector, and the remaining variables have their conventional definitions. In (32) the thermodynamic variables $\psi = (\rho,p,T,\theta)$ have been separated into two components as $\psi = \bar{\psi}(z) + \psi'(\mathbf{x},t)$ where the overbar denotes a background state of hydrostatic equilibrium. In I we perturbed about a basic state which was isentropic and the model thus consisted of the so-called "deep-equations" of Ogura and Philips (1962). Since the Brunt-Väisälä frequency N, where $N^2 = (g/\bar{\theta})d\bar{\theta}/dz$, is such that $N^2 = 0$ for this basic state, the model had to be initialized at $t = 0$ with $\psi'(\mathbf{x}, t = 0) = \psi'(z)$ in order that the atmosphere be able to support the propagation of internal waves. For the present applications this approach must be rejected since we are interested in studying the propagation of the gravity wave through realistic atmospheres in which there are extreme vertical variations of potential temperature between the troposphere and the lower stratosphere. If we were to write the perturbation equations in terms of deviations from an isentropic state the initial $\psi'(z, t = 0)$ would have to be large and the additional fluctuations associated with the wave could be strongly affected by truncation error.

To remedy this defect we have elected to rewrite the calculation in terms of deviations from a hydrostatic reference state in which the potential temperature profile $\bar{\theta}(z)$ is an exponentially increasing function of z. To determine the inverse scale height S of this profile we fit a least-squares straight line to the data obtained from an upstream sounding and constrain the fit to give the observed potential temperature at the surface. The fields $\bar{\psi}$ therefore have the explicit forms

$$\bar{\theta}(z) = \theta_0 \exp(Sz), \tag{33a}$$

$$\bar{p}(z) = p_0 e^{-Sz/\kappa}\left[e^{Sz} - \frac{g}{c_p T_0}\frac{(e^{Sz}-1)}{S}\right]^{1/\kappa}, \tag{33b}$$

$$\bar{\rho}(z) = \rho_0 e^{-Sz/\kappa}\left[e^{Sz} - \frac{g}{c_p T_0}\frac{(e^{Sz}-1)}{S}\right]^{(1/\kappa)-1}, \tag{33c}$$

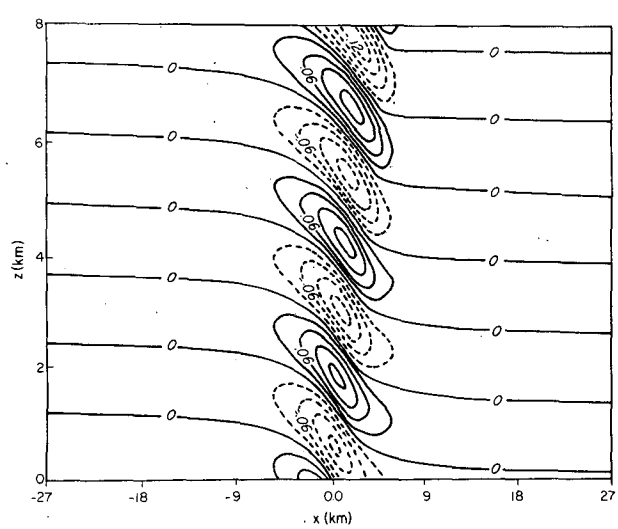

FIG. 2. Contours of constant (steady-state) vertical velocity $w(x,z)$ deduced from $\xi(x,z)$ in Fig. 2.

$$\bar{T}(z) = T_0\left[e^{Sz} - \frac{g}{c_p T_0}\frac{(e^{Sz}-1)}{S}\right], \tag{33d}$$

where p_0 and θ_0 are respectively the pressure and potential temperature on $z = 0$; $R = c_p - c_v$ is the gas constant for dry air; c_p and c_v are the specific heats at constant pressure and volume; and S is the constant (so-called) stability. In deriving (33) we have made use of the ideal gas equation of state

$$p = \rho RT, \tag{34a}$$

the definition of potential temperature

$$\theta = T(p/p_0)^{-\kappa}, \tag{34b}$$

where $\kappa = R/c_p$, and the condition for hydrostatic balance

$$\frac{dp}{dz} = -\rho g \tag{34c}$$

Through a linearization of (34a,b) we may obtain an expression for the density perturbation in (32a) as

$$\rho' = -\bar{\rho}\frac{\theta'}{\bar{\theta}} + \frac{p'}{c^2}, \tag{35}$$

where $c^2 = \gamma R\bar{T}$ is the square of the adiabatic sound speed which is clearly a function of z in the background state. Substituting (35) into (32a) and expanding $\theta = \bar{\theta}(z) + \theta'(x,t)$ we obtain a closed system in two spatial dimensions for the four variables θ', p', u, w.

The stress tensor τ_{ij} in (32a) has the usual form

$$\tau_{ij} = \bar{\rho}K_m D_{ij}, \tag{36}$$

where the deformation tensor D_{ij} is just

$$D_{ij} = \partial_j u_i + \partial_i u_j - \tfrac{2}{3}\partial_k u_k \delta_{ij}. \tag{37}$$

The heat flux vector in (32c) has components

$$H_i = \bar{\rho}K_H \frac{\partial\theta}{\partial x_i}. \tag{38}$$

In the viscous absorbing layer (see Fig. 3) we adjust τ and H_i such that diffusion acts only on perturbations from the environmental state. Since the reference state is *not* the upstream profile we must still initialize $\psi'(x,t) = \psi'(z, t = 0) \neq 0$ in order to assimilate actual upstream radiosonde observations. In I we allowed for the calculation of K_m through first-order closure and determined K_H through the assumption of unit Prandtl number $\mathrm{Pr} = K_m/K_H = 1$. In the present calculations this option is invoked only in Section 7 where the Boulder windstorm simulation is discussed. For the majority of the calculations we have assumed $K_m = K_H = 0$ (Sections 4 and 5) or $K_m = K_H =$ constant (small) as in Section 6 which concerns the description of the evolution in time of a linear resonant mode (lee wave).

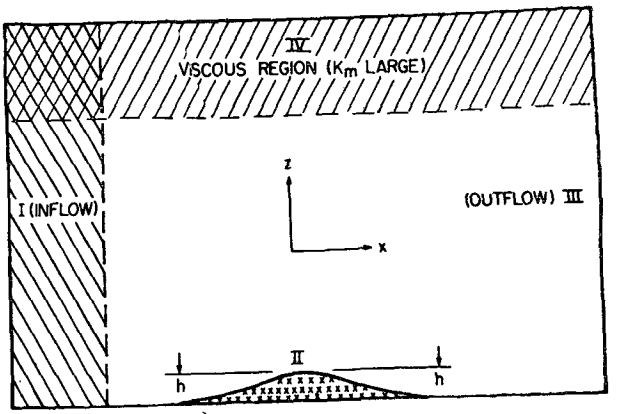

FIG. 3. Domain for the time-dependent nonlinear simulations. The hatched region denotes the volume in which dissipation is artificially enhanced to prevent reflection.

As discussed in I the important lower boundary condition is dealt with effectively by transforming the hydrodynamic equations from (x,z) to $(\bar{x},\bar{z})$ coordinates where (Gal-Chen and Sommerville, 1975)

$$\left.\begin{aligned}\bar{x} &= x\\ \bar{z} &= H\frac{z - z_s(x)}{H - z_s(x)}\end{aligned}\right\}. \tag{39}$$

In (39) H is the height of the numerical domain and $z_s(x)$ the topography. The forms of the transformed field equations are given explicitly in I and the nonlinear time-dependent system is solved numerically using standard methods described in detail in Clark (1977).

The remaining boundaries of the numerical domain are as important as the lower one. In Fig. 3 we show a schematic illustration of the region. At the overhead boundary (marked IV in the figure) we require an effective Sommerfeld condition which prevents reflection from this surface. As in I, this is effected by including a layer near the boundary in which the dissipation is gradually enhanced to a maximum at the boundary itself. The same was done near the upstream boundary (marked I in the figure) although this was not equally mandatory. At the outflow boundary we continue to employ a variant of the extrapolation scheme described by Orlanski (1976) and have found this to be an effective means of suppressing transient reflections from this region. For further details of the numerical model the interested reader should consult Clark (1977) and I.

4. High-drag and low-drag regimes in a homogeneous flow

In Fig. 4 we show the linear steady-state streamline pattern for the homogeneous model discussed at the end of Section 2 and previously in I. The forcing topography is bell-shaped with $a = 3$ km and

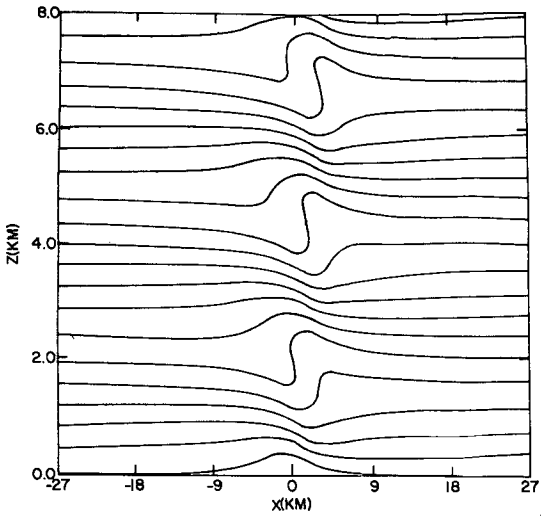

FIG. 4. Linear, steady-state, inviscid streamline pattern for the homogeneous model. The height of the mountain is 25% supercritical according to linear theory. Note that the first streamline reversal occurs at a height $z_c = 3\lambda_z/4$.

$h = 500$ m so that A exceeds A_c by 25% ($h_c = 400$ m). For this supercritical aspect ratio linear theory predicts that the streamline which "enters" at a height $z_c = 3\lambda_z/4$ above the surface has a slope which exceeds 90° directly over the mountain peak (see Fig. 4). The Froude number $\mathrm{Fr} = N^2a^2/U_0^2 \approx 60$ so that the basic wave is moderately hydrostatic while the aspect ratio $A = 1/6 > A_c = 2/15$. Note from the figure that there is a slight increase in amplitude of the streamline deflection with increasing z. This is a direct consequence of the decrease of density with height. In Fig. 5 we show the nondimensional tangential wind speed perturbation on the surface [M in Eq. (20)] for $h = 500$ m as a function of horizontal position x (dashed line). Note that this function has odd symmetry about $x = 0$ and its basic structure illustrates clearly the connection between the process of internal wave generation by topography and the downslope windstorm phenomenon. However, linear theory predicts only $M_{\max} \approx 0.64$ for $A = 1/6$ so that a "storm" as such does not exist in the linear picture since $u_{\max} \approx 6.56$ m s^{-1} from $u_{\max} = (M_{\max} + 1)U_0$. To generate a storm we require a mechanism for increasing $M_{\max}$ substantially.

Such a mechanism exists in the nonlinear dynamics. To describe it we will begin by exploring the characteristics of the flow which obtain for the full nonlinear time-dependent problem. In Fig. 6 we show a sequence of time slices through the evolving streamfield. The interior of the domain is completely inviscid and the mesh is $N\Delta x \cdot M\Delta z$, where $N = 182, M = 64, \Delta x = 600$ m, $\Delta z = 100$ m. The time step $\Delta t = 10$ s. Notice from the final frame shown in Fig. 6 that the streamline which enters at the height z_c is supercritically steepened in the region directly overhead of the mountain peak in accord with the linear prediction (cf. with Fig. 4).

In Fig. 7 we show the same time sequence of the streamfield for the same flow on a higher resolution mesh for which $\Delta x = 300$ m and the other parameters of the model are the same as above. For these calculations the horizontal resolution is double that employed for the calculation shown in Fig. 6. Furthermore, since we employ the same number of horizontal grid points as before the lateral boundaries are now located only 27 km distant from the center (as opposed to 54 km). We note again that in the final frame a critically steepened streamline exists at the height $z_c = 3\lambda_z/4 \approx 1.836$ km, so that the two calculations are in qualitative accord in this respect.

We may quantify this resolution check by comparing the surface wave drag as a function of time for the two calculations. This comparison is shown in Fig. 8. Clearly, the two calculations are in close agreement and we may therefore feel confident that neither the resolution nor the nearness of the lateral boundaries are affecting the outcome of the experiment in any significant way. The dashed

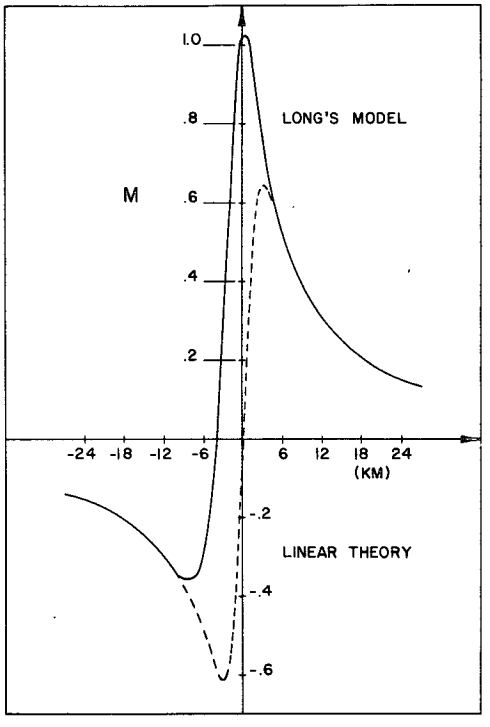

FIG. 5. Downslope wind amplification factor $M = u'/U$ for bell-shaped topography with $h = 500$ m, $a = 3$ km for (a) linear theory, dashed line, and (b) nonlinear theory (Long's model), solid line. The effective nonlinear topography has a height of only $h \approx 396$ m. Note that the effect of the nonlinear lower boundary condition is to produce a sharp increase in the strength of the downslope flow to the lee of the mountain peak.

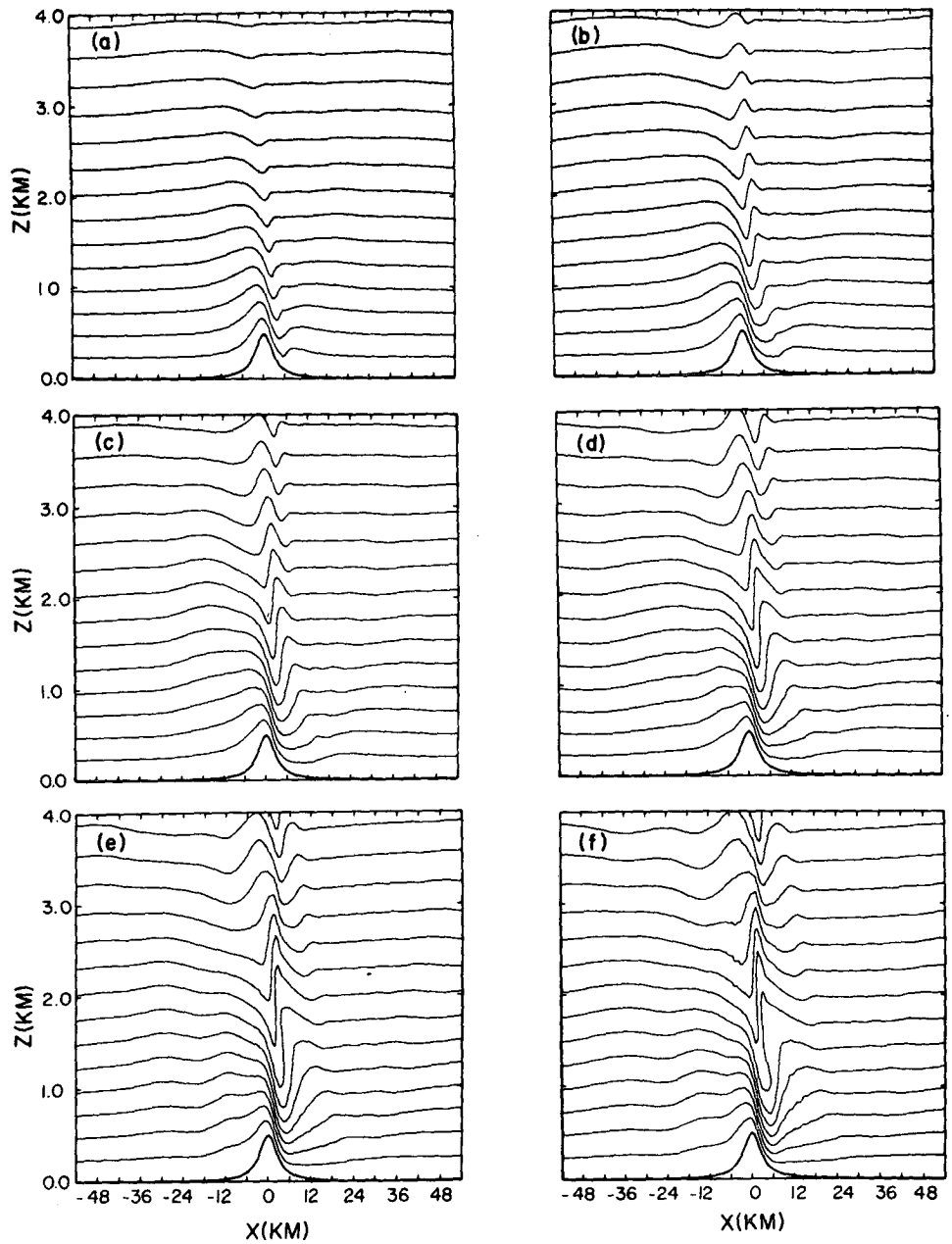

FIG. 6. Evolution in time of the streamfunction from the nonlinear simulation. The background flow is homogeneous and the topography is bell-shaped with height $h = 500$ m. The times are (a) 2400, (b) 3600, (c) 4800, (d) 6000, (e) 7200 and (f) 8400 s. Only about half of the vertical extent of the domain is shown and the mesh is low resolution.

line on the figure is the linear steady-state prediction of the surface drag and we see as in I that the surface drag increases continuously as a function of time. The regime of physical amplification follows the $200\Delta t$ startup phase in which the upstream flow is accelerated uniformly from rest to its steady 4 m s^{-1} amplitude. Since $\Delta t = 10$ s this startup phase is 33.3 min long (about three Brunt periods) and is introduced to reduce the amplitude of the transients generated by initialization as discussed in I. For this model, amplification ceases after about 900 time steps which is the time at which the streamline reversal actually occurs.

We see, then, that for $A > A_c$ there is a transition away from the low-drag state which is predicted by linear theory and that this transition is independent of resolution, independent of the nearness of the lateral boundaries, and more importantly

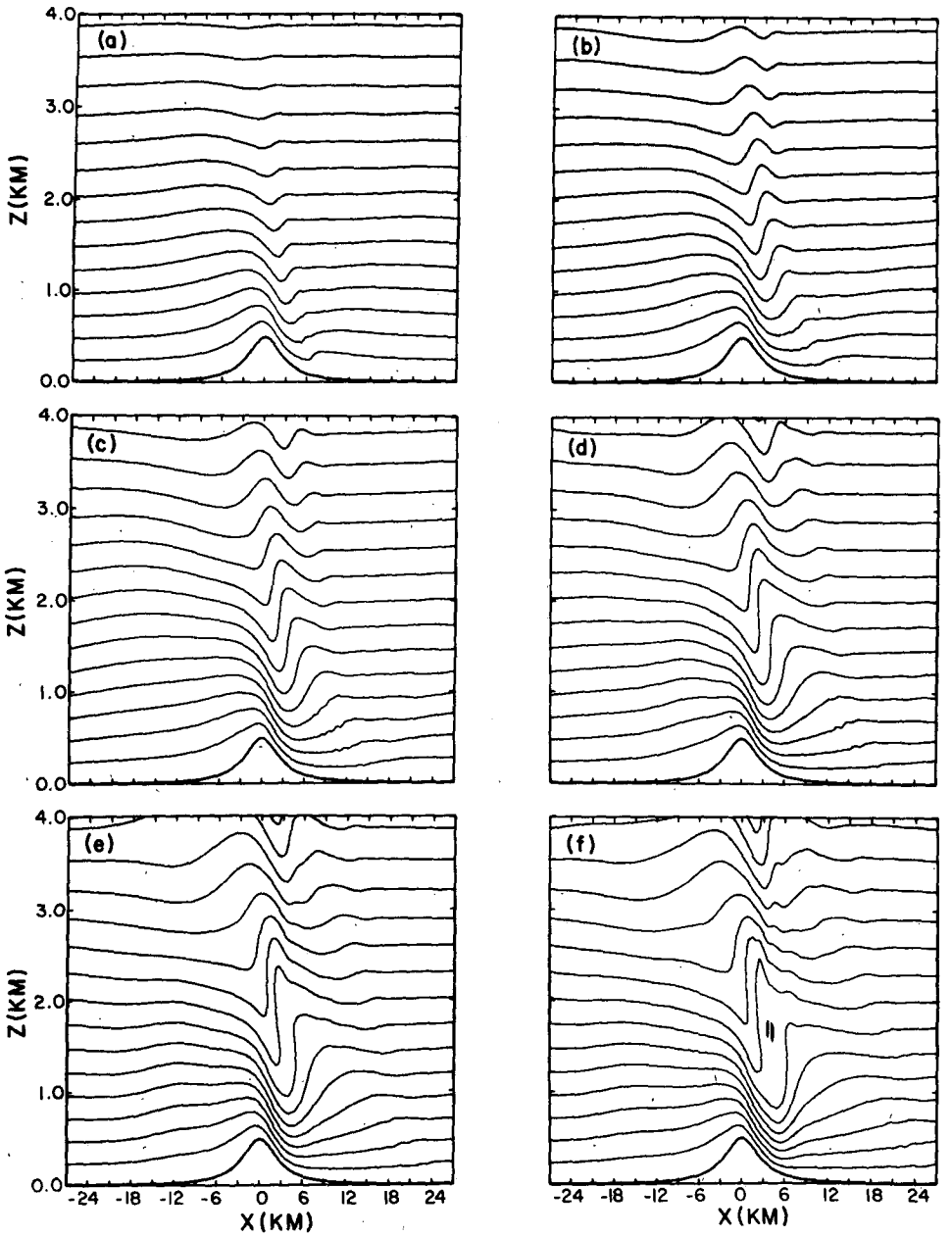

FIG. 7. As in Fig. 6 at identical times but with high horizontal resolution.

it is not dependent on spurious effects due to the parameterized diffusion introduced in I for $A > A_c$. We have previously shown that for $A < A_c$ and in the limit $t \to \infty$ a steady state is eventually obtained from the nonlinear time-dependent calculations which is essentially identical to that predicted by linear theory. We have also shown in I that for $A < A_c$ the Reynolds stress in the interior is nondivergent as it should be for sufficiently small wave amplitude. The calculations described here simply confirm the result obtained in *I*, that for $A \gtrsim A_c$ the linear solution becomes irrelevant as it differs markedly from its nonlinear counterpart. The surface drag in the nonlinear regime is enormously in excess (~300%) of the linear prediction even though the aspect ratio is only moderately (~25%) in excess of the critical value predicted by linear steady-state theory.

In Fig. 9 we show the evolution in time of the nondimensional perturbation tangential wind speed on the surface $(u_T - U_0)/U_0$ which is the nonlinear analogue of the function M shown previously for the linear model in Fig. 5. Note that the maximum tangential wind speed in the lee is continuously

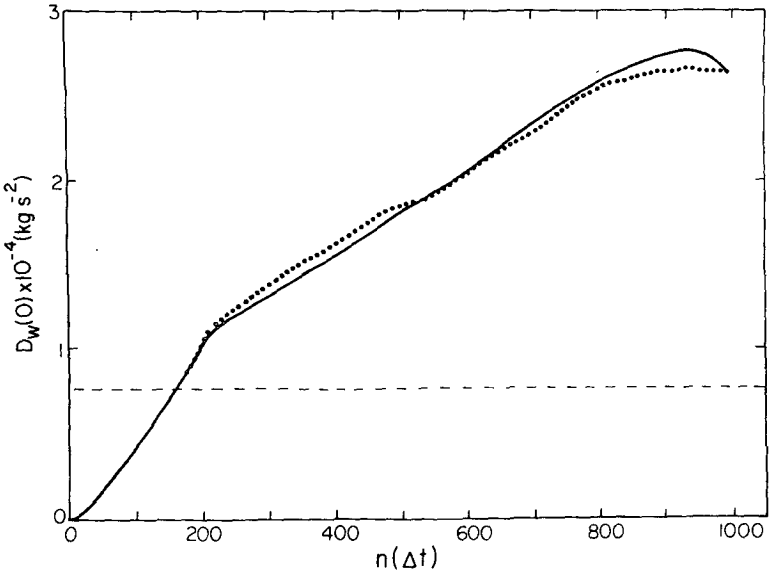

FIG. 8. Surface drag $D_w(0)$ as a function of time for the low- and high-resolution simulations shown in Figs. 6 and 7, respectively. Time is measured in the number (n) of timesteps (Δt = 10 s). Solid line is low resolution.

increasing as a function of time and for the latest time shown (~2.4 h) u'/U_0 is about 2.4 times the linear maximum. The increase of the maximum downslope wind speed above the linear prediction is in accord with the amplification of the wave drag (see Fig. 8). That this should be the case follows from the definition $D_w(0) = \overline{\rho_0 u' w'}$. Since w' is fixed by the lower boundary condition the growth of $D_w(0)$ implies a coherent growth of u' and this implies a coherent growth of $M = u'/U_0$. In the course of its transition from the low-drag to the high-drag state a downslope wind storm develops in the lee of the tropography. The maximum wind speed in the late times is seen by inspection of Fig. 9 to be on the order of 12.5 m s^{-1} which is in excess of three times the mean flow speed. The storm generation capability of the nonlinear model is thus clear.

Before considering the physical mechanism which underlies the transition from the low-drag to the high-drag regime we wish to further illustrate the fact that this transition turns out to be rather abrupt. We shall do this by calculating a quantity $R(\mathrm{Fr},A)$ which is a nondimensional measure of the rate at which the surface drag grows following the 200 Δt startup period. R is determined from the time evolution of the surface wave drag following startup according to the definition

$$R(\mathrm{Fr},A) = \frac{\tau}{D_w^{t_s}(0)}\left(\frac{\partial D_w(0)}{\partial t}\right)_{t>t_s}, \qquad (40)$$

where t_s = 200 Δt is the time at the end of the startup phase of an experiment at fixed Fr and A, and where τ is the two-way group delay of the disturbance between the ground and the first steepening level. The choice of the time scale τ for nondimensionalization is essentially arbitrary but we do wish momentarily to call attention to the long time scale required to establish the region of reversed streamlines and so the linear group delay between this region and the ground is convenient.

To calculate $R(\mathrm{Fr},A)$ we require τ and this may be obtained as follows. The Boussinesq form of the plane wave dispersion relation is

$$k_z^2 = k_x^2\left(\frac{N^2}{\omega^2} - 1\right), \qquad (41)$$

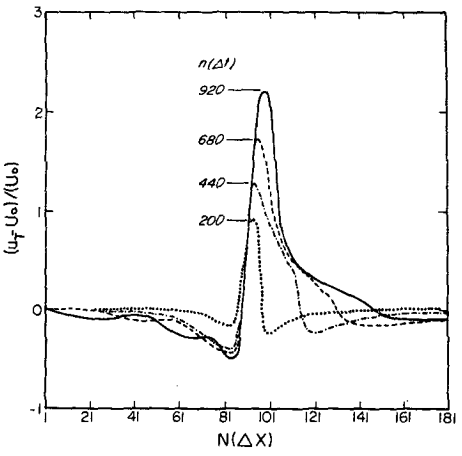

FIG. 9. Evolution in time of the perturbation tangential wind speed on the surface $\tilde{z}$ = 0. This should be compared to the appropriately scaled Long's model result shown previously in Fig. 5. Note the continuous increase in time of the downslope wind maximum to the lee of the peak.

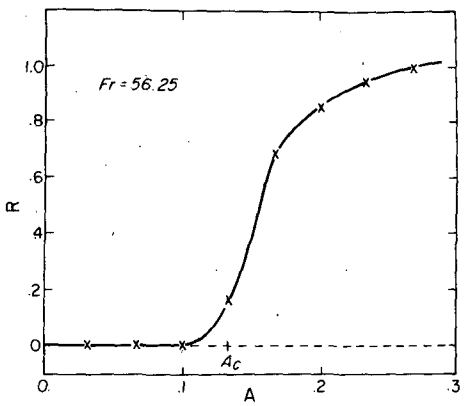

FIG. 10. $R(A)$ for fixed Froude number Fr $\approx$ 56.25. A_c is the critical aspect ratio predicted by linear theory.

from which we may obtain the vertical component of the group velocity as

$$V_{G_z} = \frac{\partial \omega}{\partial k_z} = \frac{-\omega k_z}{(k_x^2 + k_z^2)} . \tag{42}$$

The distance between the ground and the first steepening level for a hydrostatic disturbance is $z_c = 3\lambda_z/4$, so that the length of the two-way path is $D = 3\lambda_z/2 = 3\pi/k_z$. The two-way group delay is then

$$\tau = \frac{D}{V_{G_z}} = \frac{3\pi}{k_z} \frac{(k_x^2 + k_z^2)}{\omega k_z}$$

$$= \frac{3\pi}{\omega} \frac{\mathrm{Fr}}{a^2 k_z^2} . \tag{43}$$

For a hydrostatic disturbance $k_z^2 \approx N^2/U^2$, thus $\tau = 3\pi/\omega$. Since the steady disturbance launched by the mountain has $\omega = k_x U$ and since the dominant horizontal scale in the wave packet is $\lambda = 2\pi/k_x \approx 2a$, in the hydrostatic regime we thus have $\tau \approx 3a/U$. In the nonhydrostatic regime, as Fr $\rightarrow 1^+$, $k_z \rightarrow 0$ and therefore from (44) $\tau \rightarrow \infty$. In the strongly nonhydrostatic regime we have found no evidence of amplification, and indeed, in this regime (Fr $\ll 1$) the wave drag is identically zero. In Fig. 10 we show a plot of $R(\mathrm{Fr},A)$ at Fr = 56.25 for which the forced wave is moderately hydrostatic. The transition near A_c is rather abrupt. In the region $A < A_c$ the wave drag is very near the linear prediction, while in the region $A > A_c$ the wave drag in the long time limit is very much in excess of linear.

Comparing Figs. 7 and 8 we note an additional characteristic of the evolution of the disturbance in the nonlinear regime. The time taken for the flow to become fully developed at the first steepening level $z_c = 3\lambda_z/4$ is about 900 $\Delta t = 9 \times 10^3$ s. From the preceding analysis, however, the one-way group delay between $z = 0$ and $z = z_c$ is $t \approx 3a/2U = 1.125 \times 10^3$ s. Clearly, in the nonlinear regime, the time required for the flow to develop fully at a given level is very much longer than linear theory would suggest. From the results in I, on the other hand, the steady-state flow at a given level is established on the linear time scale if $A < A_c$. The nonlinear regime is therefore characterized not only by a marked increase in surface wave drag but also by an equally marked stretching of the governing time scale.

The first of these effects is explicable in terms of Long's model which applies to the homogeneous flow which is of interest to us here and provides an exact steady-state solution for subcritically steepened waves. The essence of Long's model is that the solution of the *linear* wave equation which satisfies the "nonlinear" lower boundary condition is the exact solution to the complete nonlinear steady-state problem. The extent to which linear theory deviates from nonlinear theory for the same obstacle may therefore be assessed by determining the extent to which the linear streamfunction (18) corresponds to the actual shape of the topography. Inspection of Fig. 4 clearly illustrates the idea. We have done linear theory for a bell-shaped obstacle of height 500 m but the low-level streamline has a net vertical deflection of only about 396 m although it has approximately maintained its bell-shaped form. This linear solution is therefore the complete nonlinear solution for a bell-shaped mountain 396 m high. Since the drag for the bell-shaped topography depends on the square of the mountain height we must expect linear theory to underestimate the wave drag by a factor of about $(500/396)^2 \approx 1.6$. Inspection of Fig. 8 confirms that this is near the ratio of the actual to the linear wave drag which obtains in the long time limit. Miles and Huppert (1969) have calculated exact Long's model solutions for the bell-shaped mountain and their critical height $h_c = 0.85U/N$ is very close to our underestimate. This confirms that the effect of the distortion of the mountain shape is unimportant in our calculations.

We can see why the discrepancy in wave drag between linear theory and Long's model becomes large for aspect ratios in excess of that required to produce critically steepened waves, by employing the results from second-order theory obtained by McIntyre (1972). His work shows that the first nonlinear correction to the linear theory may be obtained by redoing the linear problem using the new topography $h'(x) = h(x)(U + u')/U$, where $u'(x)$ is the perturbation horizontal velocity on $z = 0$ obtained in a linear calculation with topography $h(x)$ (McIntyre, personal communication, 1978). This topography is both higher than $h(x)$ and asymmetric in a sense such that the surface drag is enhanced (reduced slope upwind, increased slope

downwind). This result suggests why the effect of nonlinearity should become crucial when the wave steepens to overturning. As the wave breaks, u'/U becomes of order unity and at the first steepening level $|u'| < -|U|$. The second-order correction to the topography, $(u'/U)h(x)$, is then of the same order as $h(x)$ itself and higher order effects become important. This does not demonstrate that the transition from the linear to the nonlinear regime is sharp but it does show that the transition should occur for an aspect ratio near that which is required to produce critically steepened waves. This is strikingly confirmed by the nonlinear time-dependent numerical calculations.

A second characteristic of the numerical solutions which is explained by Long's model is also evident on inspection of Figs. 4, 6 and 7. The effective Long's model solution not only corresponds to a lower mountain height than that for which the linear calculation was performed, but also the topographic maximum is shifted upstream from its linear location. As shown in Section 2, linear hydrostatic theory predicts that the critical points are located precisely over the topographic maximum for symmetric topography and that the first is located at a height $z = 3\lambda_z/4$. Fig. 4 shows that one nonlinear effect of the lower boundary condition is to shift the horizontal location of the critical point with respect to the topographic maximum without altering the height at which this region of the flow is found. Inspection of Figs. 6 and 7 provides a very nice numerical confirmation of this expected nonlinear effect. As will be shown in the next section, this effect is also evident in nonhomogeneous models.

We wish to return here to the point made above regarding the sharpness of the transition from the linear to the nonlinear regime as evidenced in the numerical calculations of surface wave drag. In Fig. 11 we have plotted surface drag versus aspect ratio both for linear theory and for an approximate version of Long's model in which the mountain height is correct but the shape correction is not included, i.e., we have not iterated the solution to find the exact linear topography which would correspond through its associated low-level streamfunction to the desired physical form of the mountain. Even though the Long's model solutions are not exact the data in Fig. 11 do show quite clearly that the transition from the low-drag to the high-drag regime is rather abrupt and occurs near A_c.

That Long's model also explains the difference between M from linear theory (dashed curve in Fig. 5) and the equivalent downslope wind amplification factor for the nonlinear model (Fig. 9) is seen clearly in Fig. 5 (solid curve). To obtain the Long's model result in Fig. 5 we have simply interpolated the u', w data from the linear calculation onto the

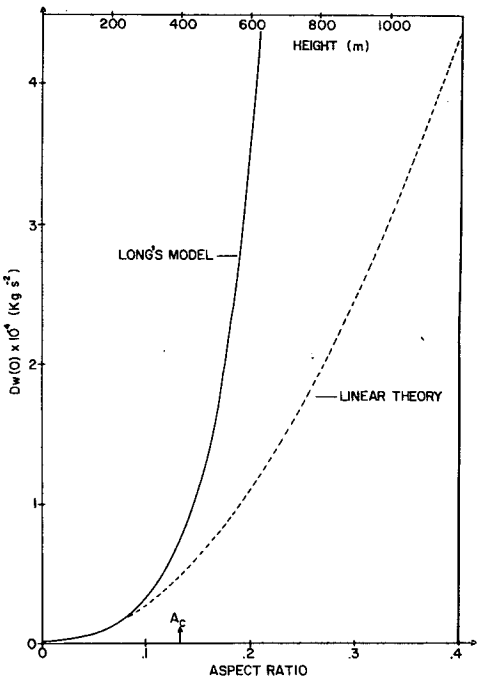

FIG. 11. Wave drag versus aspect ratio for linear theory (dashed line) and for the approximate version of Long's model discussed in the text. Note that the discrepancy becomes large for $A \gtrsim A_c$.

low-level streamline and formed $u_T = [(u'^2 + w^2)^{1/2} - U_0]/U_0$ which is the tangential wind speed on the surface which we should expect from a nonlinear calculation with mountain height $h \approx 396$ m and halfwidth $a = 3$ km. The effect of the nonlinear lower boundary condition is thus to produce a sharp increase of the downslope wind maximum in the lee of the peak when the aspect ratio of the topography is near or in excess of critical. Again this is strikingly confirmed by our nonlinear time-dependent calculations.

The only characteristic of the nonlinear time-dependent solutions for homogeneous flows which is not explicable in terms of Long's model is the previously noted long time scale required for the flow to establish its fully developed form. Since Long's theory is explicitly a steady-state theory this should not be too surprising. The explanation of the existence of this new time scale in the highly nonlinear regime is almost certainly due to the fact that as the flow develops the lower boundary condition, being nonlinear, is also changing. It should be possible to deduce the dependence of this time scale analytically but we will not attempt to do so here.

The main point which we wish to make in consequence of the results obtained in this section is the following. The effect of the nonlinear lower boundary condition in the mountain wave problem, on the surface wave drag and therefore also on

the momentum flux in the wave field, is extremely important. Furthermore, the transition from the linear or weakly nonlinear regime to the highly nonlinear regime is rather abrupt as an increasing function of aspect ratio. In the nonlinear regime the steady-state wave drag is very much in excess of the linear prediction, and related to this is the fact that the strength of the downslope flow in the lee of the topography is also enormously enhanced over the associated linear strength. This suggests an explanation of the phenomenon of intense downslope wind storms in terms of nonlinearity, and this explanation is clearly and fundamentally different from that which has been advanced by Klemp and Lilly (1975). It is doubtless true, however, that both nonlinearity and inhomogeneity of the basic state are simultaneously important and which effects dominate will depend on the specific combination of mean flow and topography which is under consideration. The interactions between these effects will be considered in the following sections.

One further point which we will mention briefly here and return to later, concerns the numerical methods which should be employed to simulate mountain wave flows in the regime of strong nonlinearity. As we have shown previously, this regime is characterized by flows in which reversed streamlines occur. Since for high Reynolds number flows streamlines are also isentropes, the region centered about the wave-induced critical level is a region in which the vertical gradient of temperature is superadiabatic. The regime of strong nonlinearity is therefore strictly inaccessible with a numerical model which is written in terms of isentropic coordinates, since the coordinate transformation is undefined in the region where the wave breaks. In Section 5 we will proceed to examine the question as to whether realistic atmospheric flows, which are strongly inhomogeneous, should be within the strongly nonlinear regime and, if so, how the effects of inhomogeneity and nonlinearity interact.

5. Downslope wind storms in a "standard" winter atmosphere

In Fig. 12 we show the profiles of wind speed and temperature which will be employed for the first simulation of transition from the low-drag to the high-drag regime under realistic atmospheric conditions. The temperature profile is for average midlatitude winter conditions and the wind field is for the mean zonal flow (e.g., Newell *et al.*, 1972). As forcing we will employ bell-shaped topography with variable height and fixed halfwidth $a = 10$ km. Fig. 13 shows the power spectrum of the linear ξ solution in wavenumber space for this forcing (with $h = 500$ m) and background state. This is just the kernel of the Fourier integral (16) multiplied by its complex conjugate and suitably normalized. Noticeable is the weak spectral peak near real wavenumber $k = 6 \times 10^{-4}$ m^{-1} which is produced by the weak excitation of a normal mode (lee wave) which has coordinates $k = (6.01 \times 10^{-4}, 1.27 \times 10^{-5})$ m^{-1} in the complex k-plane. That this mode is not a prominent feature of the complete linear solution can be seen in Fig. 14 where we plot the free-stream deflection $\xi(x,z)$ obtained by fast Fourier inversion of the complex k-spectrum as described in Section 2. The linear solution is strongly dominated by the freely propagating hydrostatic part of the spectrum.

From the field $\xi(x,z)$ we can compute the stability index I_2 defined in (25) and since ξ scales linearly with the height h of the mountain we can determine the height h_c required to satisfy condition (26). This gives $h_c \approx 590$ m and therefore the critical aspect ratio for this flow is $A_c \approx 0.059$. Fig. 15 illustrates the linear steady-state streamline pattern for a slightly supercritical aspect ratio $A = 0.0625 > A_c$. Note that the critical point again

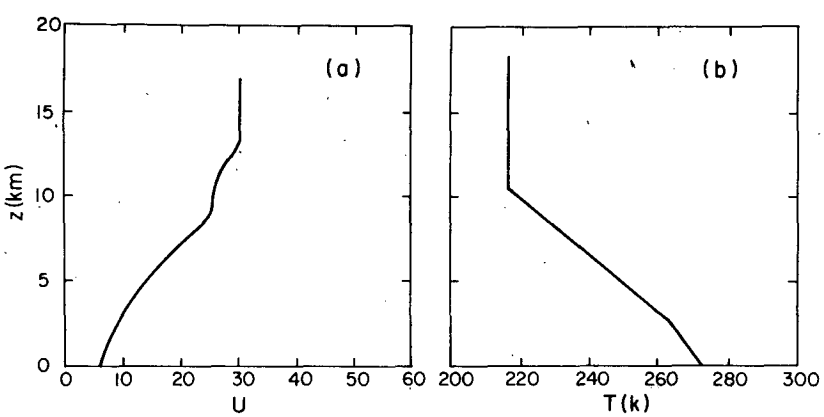

FIG. 12. Wind speed (a) and temperature (b) as a function of height for average midlatitude winter conditions.

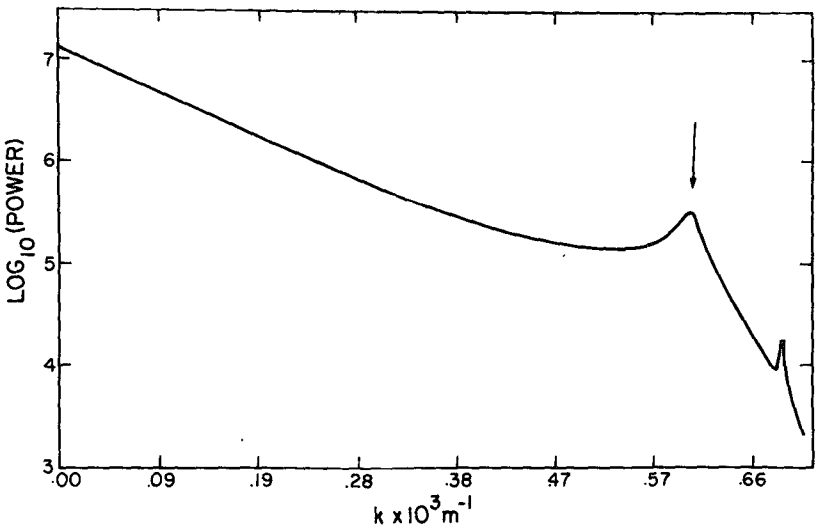

FIG. 13. Wavenumber spectrum of the linear solution at height $z \approx 4$ km for the midlatitude winter conditions shown in Fig. 13. The topographic forcing is bell-shaped with $a = 10$ km and $h = 500$ m.

occurs at a height approximately 2 km above the surface as for the simple homogeneous model described in the last section. The integrated phase shift between the ground and the wave-induced critical layer is $3\pi/2$ in agreement with Eq. (20). Unlike the solution for the homogeneous flow shown in Fig. 4, that for the inhomogeneous model does not exhibit a sequence of equally spaced critical points in the vertical. This is simply a consequence of the increase of mean horizontal wind speed with height which leads to a strong increase with height of the *local* vertical wavelength. Although Long's model cannot be applied to this problem in which the background flow is inhomogeneous, it is nevertheless clear from Fig. 15 that many of the characteristics of Long's model solutions should also obtain in this case. Inspection of the low-level streamline shows that the effective nonlinear topography is lower than that used for the linear calculation and that the peak is shifted upstream

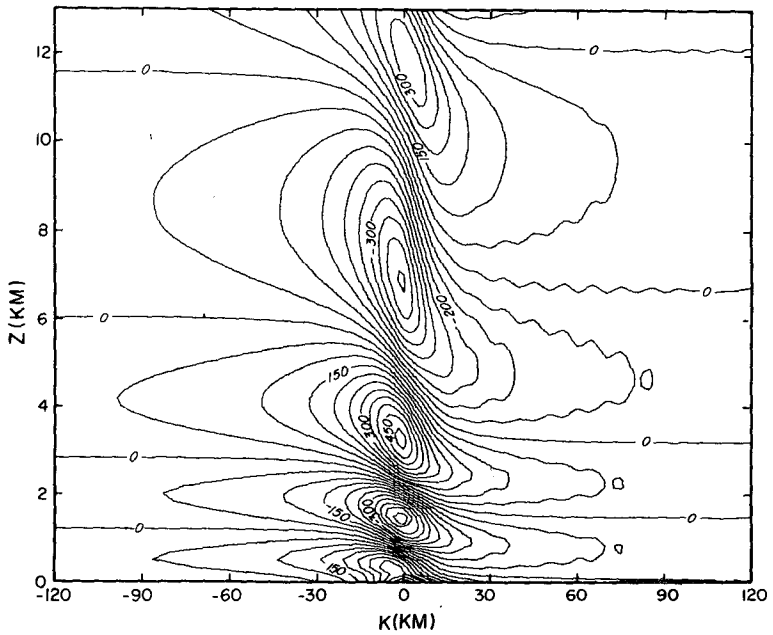

FIG. 14. Free-stream deflection $\xi(x,z)$ for the standard midlatitude winter model. Topography has $a = 10$ km, $h = 500$ m.

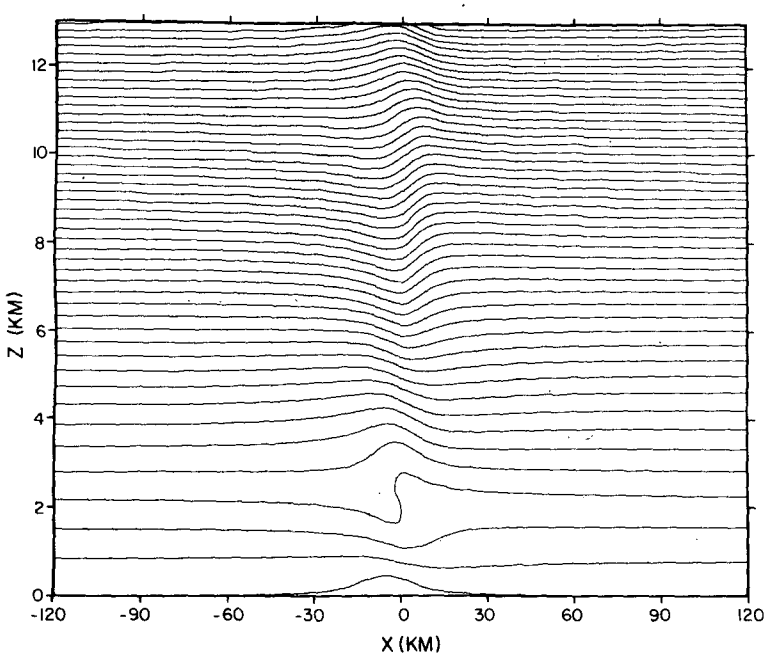

FIG. 15. Linear steady-state streamline pattern for the standard midlatitude winter model. The topographic aspect ratio is slightly supercritical. Note the overturned streamline at the critical height $z_c = 3\lambda_z/4$.

from its linear location ($x = 0$). The critical point, however, is still located immediately above $x = 0$ so that the two points are laterally displaced as for the previous homogeneous flow.

It should be recognized that the critical aspect ratio $A_c = 0.059$ is rather small, in particular it is smaller than the aspect ratio $A \approx 0.2$ of the topography to the west of Boulder, Colorado (for which $a \approx 10$ km, $h \approx 2$ km). This region should therefore be particularly susceptible to the occurrence of downslope wind storms according to the nonlinear hypothesis for their formation and this is observed to be the case. The same is true of the topography of the Rocky Mountains in southern Alberta to the west of the city of Calgary where the frequency of occurrence of Chinook-type winds is observed to be extremely high during the winter months (Lester, 1976).

In order to test the above predictions of linear steady-state theory, we have initialized the nonlinear time-dependent model with the same midlatitude winter profiles of wind speed and stability. In Fig. 16 we show a sequence of time slices through the streamfunction field for supercritical conditions with $h = 1$ km. For these numerical calculations the domain is $N\Delta x \cdot M\Delta z$, where $N = 182$, $M = 84$, $\Delta x = 10^3$ m, $\Delta z = 341$ m, so that the domain is 180 km long and 30 km high. The time step is $\Delta t = 7.5$ s. Inspection of the figure confirms that the streamline which enters the domain at a height $z \approx 2$ km eventually reverses.

In Figs. 17a–17c we show the temporal evolution of the surface wave drag $D_w(0)$ for three experiments which differ only in the mountain height. In Fig. 17a $h = 500$ m (linearly subcritical), while in Figs. 17b and 17c the mountain heights are respectively $h = 1$ km and $h = 1.4$ km (both linearly supercritical). On each figure the horizontal dashed line is the prediction of linear steady-state theory. We again note that in the (linearly) subcritical case the wave drag shows no strong tendency to amplify on a long time scale but does exhibit a weak tendency to do so. Clearly, this is because, as in the case of flows to which Long's model applies, linear theory provides an effectively nonlinear solution, but for a mountain whose height is lower than that employed for the linear calculation.

The two experiments in the linearly supercritical region (Figs. 18b and 18c) again show the strong and continuous amplification which is characteristic of the long time scale transition to the high-drag state, just as for the homogeneous model. After an elapsed time following startup of approximately 1.5 h the surface drag for $h = 1$ km is in excess of three times the linear prediction and the increased surface drag is accompanied by a similar increase in the tangential wind maximum to the lee of the peak. In Fig. 18c for the $h = 1.4$ km case the wave drag is more than six times larger than the linear prediction and the maximum tangential wind speeds in the lee are of hurricane force. It should be recalled that this topography is still 600 m lower than that to the west of Boulder!

Because of the complete absence of dissipation in the flow, as time proceeds beyond the final frame in Fig. 16 the coherence of the wave field

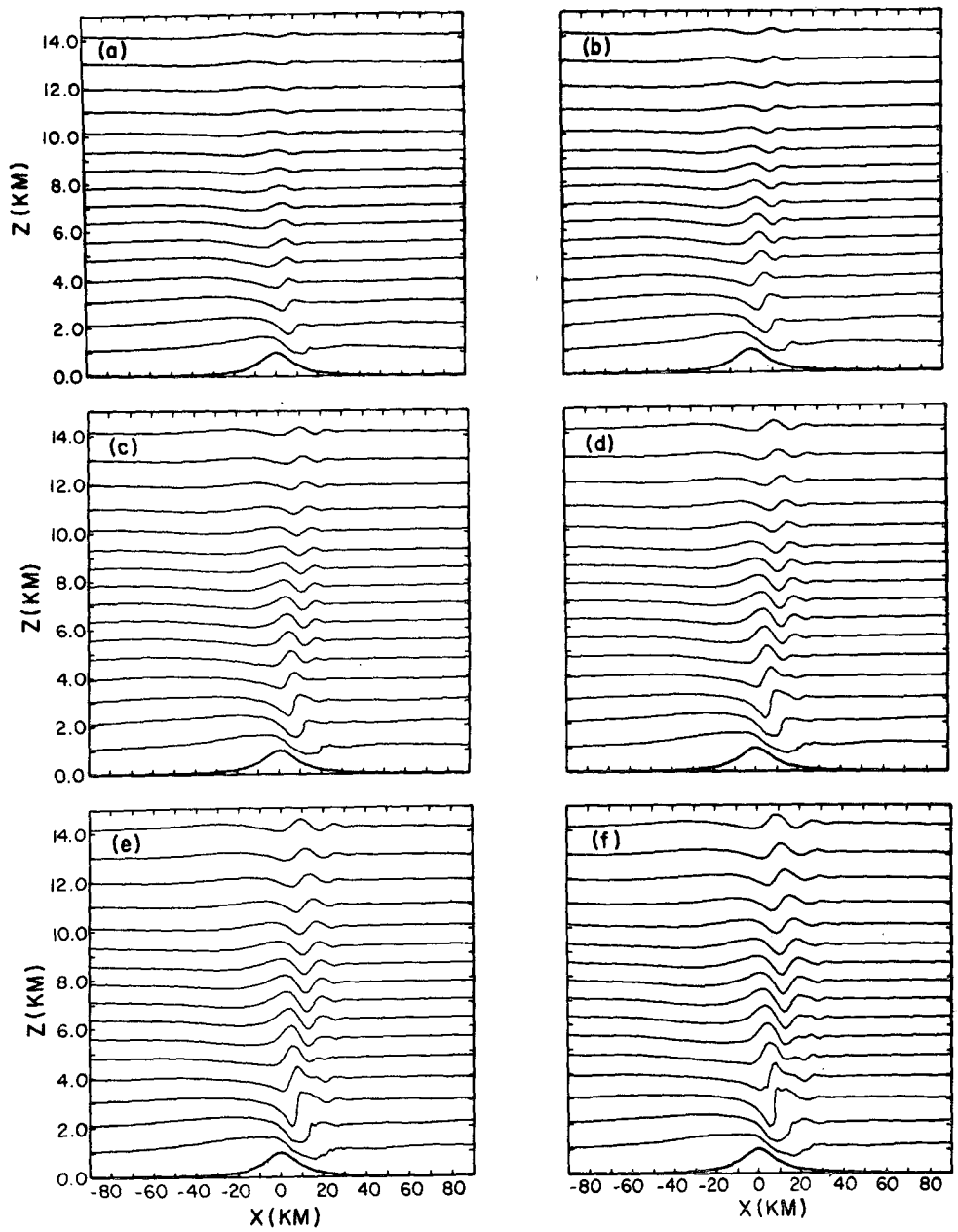

FIG. 16. Nonlinear, time-dependent evolution of the streamline field for the standard mid-latitude winter model. The bell-shaped topography has a = 10 km, and h = 1 km. The times shown are (a) 3000, (b) 3600, (c) 4200, (d) 4800, (e) 5400 and (f) 6000 s.

degrades near the steepening level (this will be illustrated explicitly in Fig. 28) where the streamlines overturn. In this region where the temperature gradient becomes superadiabatic we expect that the enhanced local mixing produced by convection will eventually quell the amplification. In I we introduced local mixing in this region via first-order closure, while we have purposely avoided introducing any mixing in the present case so that the transition to the high-drag regime could not be attributed to it.

6. The transient evolution of nonlinear lee waves

In the last section we remarked on the existence in the complete linear solution of a weakly excited normal mode (lee wave). This normal mode may be made a more prominent feature of the wave field by forcing it with a narrower topography, the width of which is matched more closely with the normal mode wavelength. Alternatively, we may keep the width of the topography fixed but alter the background profiles of wind speed and stability in such a

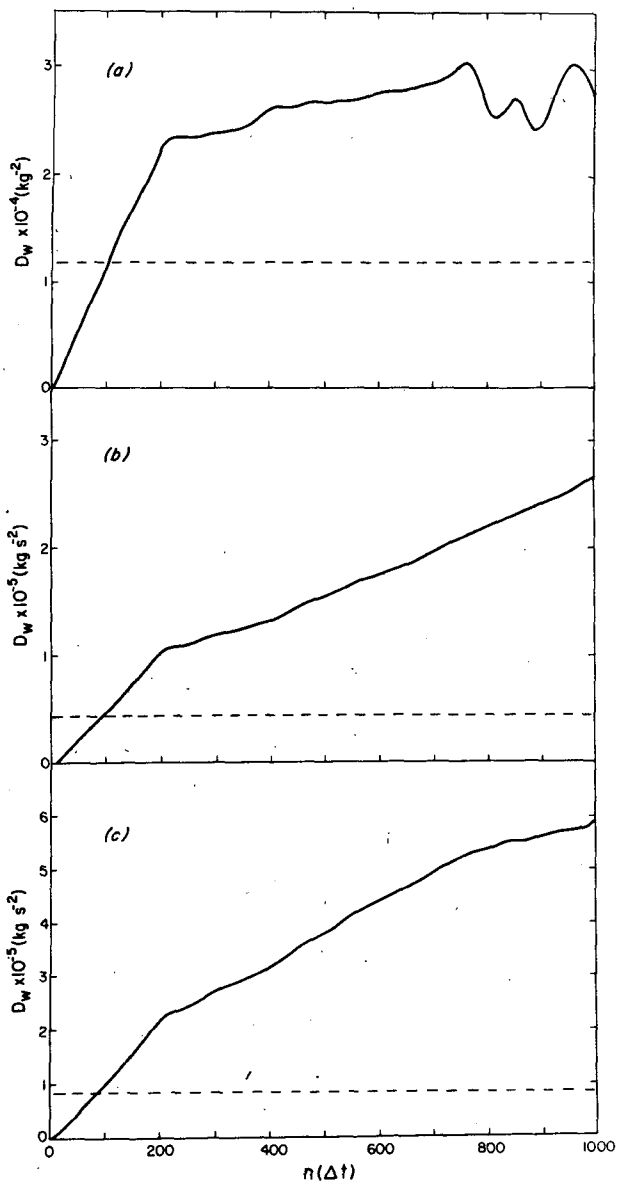

FIG. 17. Evolution in time of the surface wave drag for three nonlinear simulations with standard midlatitude winter background conditions. The topography is bell-shaped with halfwidth 10 km and the mountain heights are (a) 500 m, (b) 1 km and (c) 1.4 km.

way that the wavelength of the normal mode increases, and thereby achieve the same improved match between the scale of the forcing and of the mode. Here we follow the second route and employ the new basic-state profiles shown in Fig. 18. In Fig. 19 we illustrate the horizontal wavenumber spectrum of the ξ solution at a height $z = 4$ km for bell-shaped topography with $a = 10$ km and $h = 500$ m as in the last section. We note the presence in the power spectrum of a sharp line at $k = 3.74 \times 10^{-4}$ m^{-1} corresponding to a lee wave with horizontal wavelength $\lambda \approx 16.8$ km. Inspection of the secular function (17) in the complex k-plane shows that the pole has coordinates $k = (3.74 \times 10^{-4}, 4.09 \times 10^{-6})$ m^{-1} so that the downstream attenuation is weak, the disturbance decaying by a factor of e in a distance on the order of 1.54×10^3 km. Fast Fourier inversion of the wavenumber spectrum gives the $\xi(x,z)$ field shown in Fig. 20, which clearly shows the dominant contribution of the lee wave to the structure of the wave field. Nonhydrostatic effects are therefore extremely important in this linear model.

In view of the nonlinear transition which we have discussed in the past sections we should be concerned that the nonlinear flow may depart significantly from the linear version described above. Again we may employ the linear steady-state criterion (26) to estimate the transition point and for this flow we obtain $A_c \approx 0.4$. This implies that a bell-shaped mountain with halfwidth $a = 10$ km should be in excess of 4 km high *if* the linear condition for transition is to be satisfied. For this flow linear theory predicts that the nonlinear critical layer should form at $z_c \approx 11$ km over the mountain peak and this height satisfies the integral phase shift condition (30) of WKB theory. Inspection of Fig. 18 shows that the critical point is located just above the tropopause. In Fig. 21 we illustrate the linear streamfunction for slightly supercritical conditions and inspection reveals overturned streamlines at height $z = z_c$. This height is very much in excess of the critical point height for either of the two flows analyzed previously, which is due to the fact that the wind intensity throughout the troposphere (large) and the tropospheric stability (small) are such that the mean vertical wavelength in the troposphere is very much increased. The local vertical wavelength sharply *decreases* in the stratosphere, however, so that the distance between the critical point and the ground is still $z_c = 3\bar{\lambda}_z/4$, where $\bar{\lambda}_z$ is the mean vertical wavelength in accord with (30) as mentioned above.

Before continuing with the discussion of the nonlinear evolution of the flow described above, there are several points which we wish to make as clearly as possible since these are critical to the proper appreciation of the arguments which follow in this and the next section. First, we wish to point out that the critical aspect ratio $A_c \approx 0.4$ predicted by linear theory is large, very much larger than those which obtained for the previously discussed flows. This is a reflection of the fact that the aspect ratio is not the best scaling length for discussions of wave breaking. As shown by Miles and Huppert (1969) the natural scale for homogeneous flows is the ratio of the mountain height h to the vertical hydrostatic wavelength U/N. Given, as pointed out in the last section, that the nonlinearity of the lower boundary condition contributes *constructively*

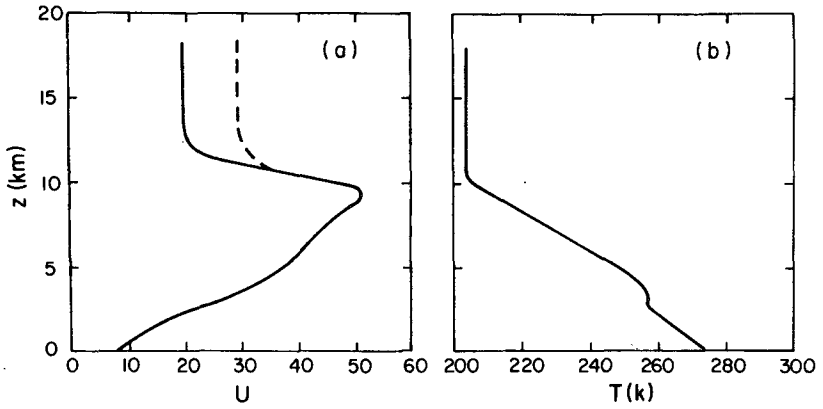

FIG. 18. Wind speed (a) and temperature (b) as a function of height for "extreme" midwinter conditions. The heavy line in (a) is the upstream wind profile which accompanied the strong downslope windstorm at Boulder. The dashed line describes the modification to it which will be employed in this section for the lee wave simulation.

(Smith, 1977) to the steepening of the wave, we may reasonably expect that the flow will enter the strongly nonlinear regime for an aspect ratio considerably lower than that predicted by linear theory for the flow of interest to us here. Indeed, and as shown in Section 7, this turns out to be the case. The second point concerns the origin of the wind and temperature profiles shown in Fig. 18. These are from the Grand Junction sounding upstream of Boulder on 11 January 1972 and are therefore the background profiles which obtained during the dramatic Boulder wind storm of that date (Lilly and Zipser, 1972). It should be immediately clear by inspection of the linear streamfunction shown previously that linear theory fails dramatically to predict the huge wave amplitudes which obtained during this storm (see Fig. 27 in the next section where the observed potential temperature field is reproduced). *In the next section we will show that this storm is a consequence of nonlinear effects which occur due to the actual breaking of the wave in the lower stratosphere.*

Here what we wish to do is modify the observed basic wind profile in such a way that wave breaking is suppressed. This will allow us to first consider a situation in which the nonlinear development of the lee wave mode may be studied in isolation from the instability. Clearly the simplest modification which will *prevent* instability is to *increase* the asymptotic stratospheric wind speed from the observed value

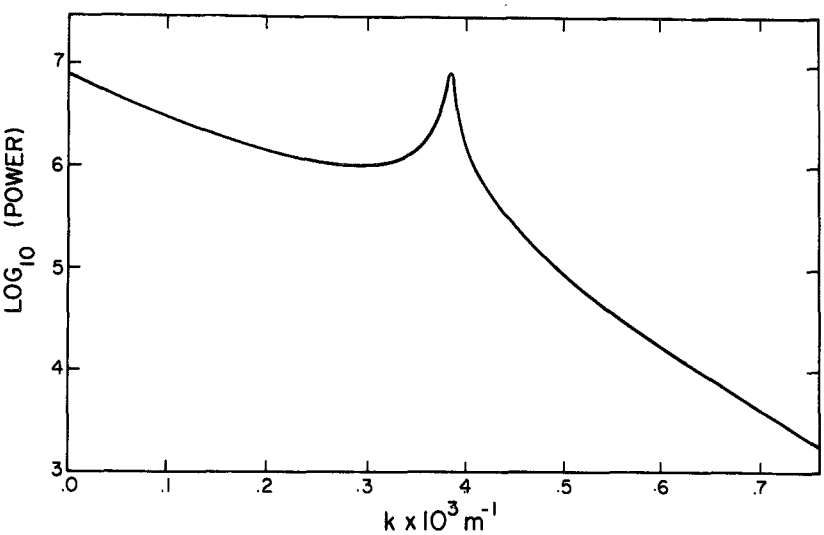

FIG. 19. Wavenumber spectrum of the linear inviscid solution for the ξ field at the height $z = 4$ km. Note the sharp resonant line near wavenumber $k = 3.75 \times 10^{-4}$ m^{-1}.

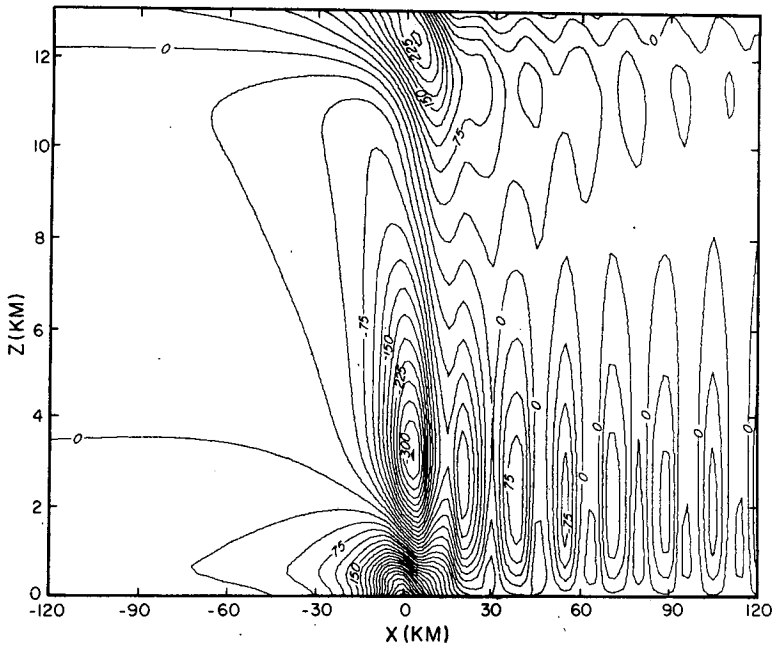

FIG. 20. Free-stream deflection $\xi(x,z)$ for the extreme midwinter model. The topography is bell-shaped with $a = 10$ km and $h = 500$ m. Note the downstream oscillation (lee wave) with wavelength $\lambda \approx 16.8$ km.

$U_s \approx 20$ m s^{-1} to some larger value since it is in the stratosphere that the critical level forms. Using bell-shaped topography with $a = 10$ km and $h = 2$ km in reasonable accord with the topography west of Boulder, we have found that an asymptotic wind speed of $U_s = 30.4$ m s^{-1} is sufficient to prevent breaking during the development of the lee wave. The complete wind profile to be employed in the numerical experiments corresponds to the dashed line in Fig. 18 and the temperature profile is unchanged from the observed.

Fig. 22 shows the surface drag as a function of

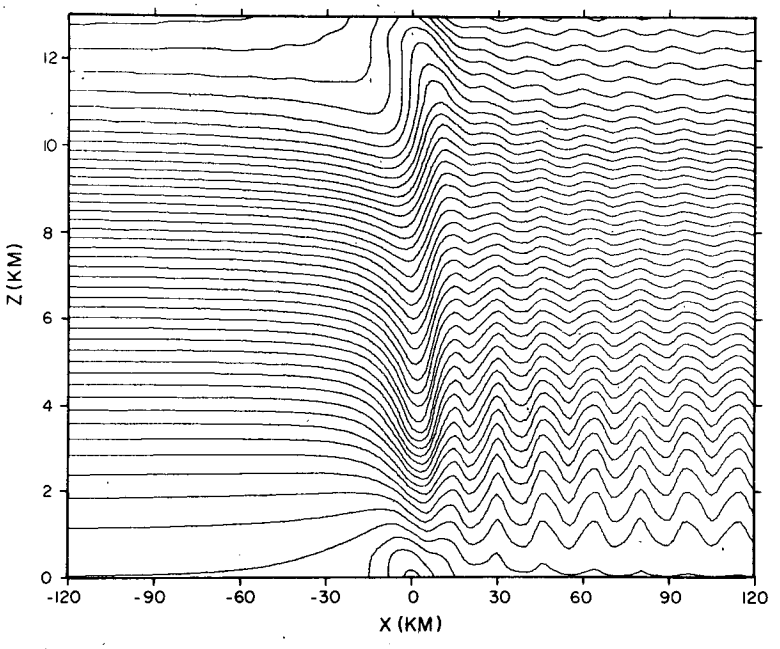

FIG. 21. Linear streamfunction for slightly supercritical conditions. Note the presence of overturned streamlines at the critical height $z_c \approx 11$ km. Note the large error in the streamfunction near the ground due to the assumed linearity of the surface boundary condition.

time for the nonlinear experiment initialized with these modified profiles. The mesh is $N\Delta x \cdot M\Delta z$, where $N = 256$, $M = 84$, $\Delta x = 500$ m and $\Delta z = 341$ m, so that the domain is 128 km long and ~30 km high. The time step $\Delta t = 7.5$ s. Because of the intensity of the response we have introduced a small amount of background mixing with K_m constant everywhere in the domain. This increases the numerical stability of the calculation but does not lead to any significant attenuation of the wave. Evident by inspection of Fig. 22 is the fact that there is no tendency for amplification following the initial startup period. Note, however, that although there is no amplification for $t > 200\Delta t$ the surface drag is very much in excess of the linear prediction, in fact by a factor of about 6.

In Fig. 23 we show several time slices through the evolving *vertical velocity* field. This illustrates very clearly the way in which the normal mode is excited as a function of time through the process of continuous partial reflection from the shear layer and total reflection from the ground. The last plate in this figure may be compared to Fig. 24 in which we show the linear steady-state prediction of the vertical velocity field. We note that the horizontal wavelength of the lee wave in the nonlinear model ($\lambda_x \approx 17$ km) is almost identical to that predicted by linear theory although the amplitude is very much larger (maximum vertical velocity ~8 m s^{-1} whereas the linear maximum is only ~1 m s^{-1}). It appears, therefore, that the excitation efficiency of the lee wave is strongly affected by nonlinearity—the nonlinear efficiency being higher than that suggested by linear theory (e.g., see Smith, 1976).

To complete our discussion of this modified flow in which the lee wave is such a prominent feature, we show in Fig. 25a the streamfunction from the nonlinear calculation and for the latest time. This may be compared with Fig. 21 from a similar but supercritical linear calculation. An interesting and important point to notice here is that the nonlinear streamfield near the steepening level at $z_c \approx 11$ km just above the tropopause is very close to overturning and the wave is therefore about to break. This is true in spite of the fact that the mountain height $h = 2$ km is about a factor of 4 smaller than the critical mountain height predicted by linear theory for the modified flow. The nearness of the wave to breaking is also evident in the isentrope field in Fig. 25b for the time corresponding to the streamfunction. Fig. 25b may be compared to Fig. 26, which shows the observed isentrope field on the occasion of the 11 January 1972 windstorm at Boulder. The storm occurred in a background state which differed from that which we have just employed for our lee wave simulation only in that the stratospheric windspeed was 20 m s^{-1} rather than 30.4 m s^{-1}. Yet comparing Figs. 25b and 26, we see that they bear no resemblance to one another at all. In the next section we shall show that additional nonlinear effects which occur when the wave breaks transform the structure of the wavefield completely and thereby lead to the formation of an intense downslope wind storm.

7. The 11 January 1972 severe downslope wind storm in Boulder, Colorado

The observational data for this and similar wind storms have been discussed many times by Lilly and his co-workers in the past several years (e.g., Lilly and Zipser, 1972; Lilly and Kennedy, 1973; Klemp and Lilly, 1975, 1978; Lilly, 1978; Smith,

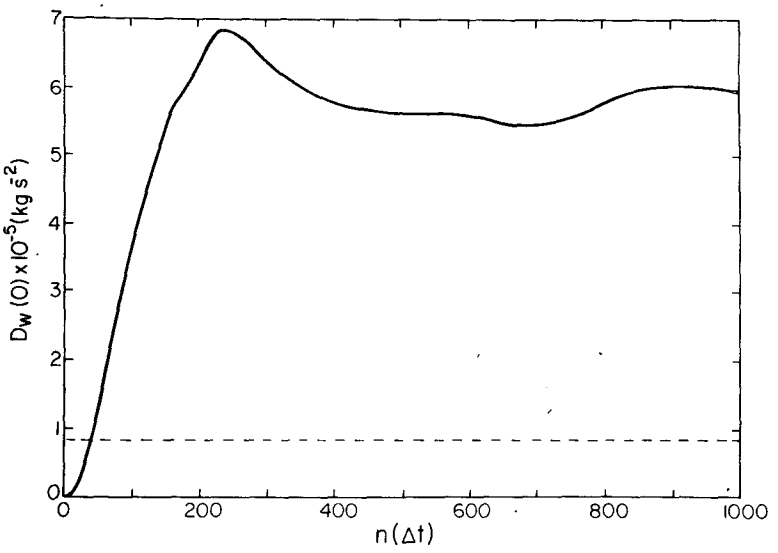

FIG. 22. Surface wave drag $D_w(0)$ as a function of time for the extreme winter model with the background wind profile modified as shown in Fig. 18.

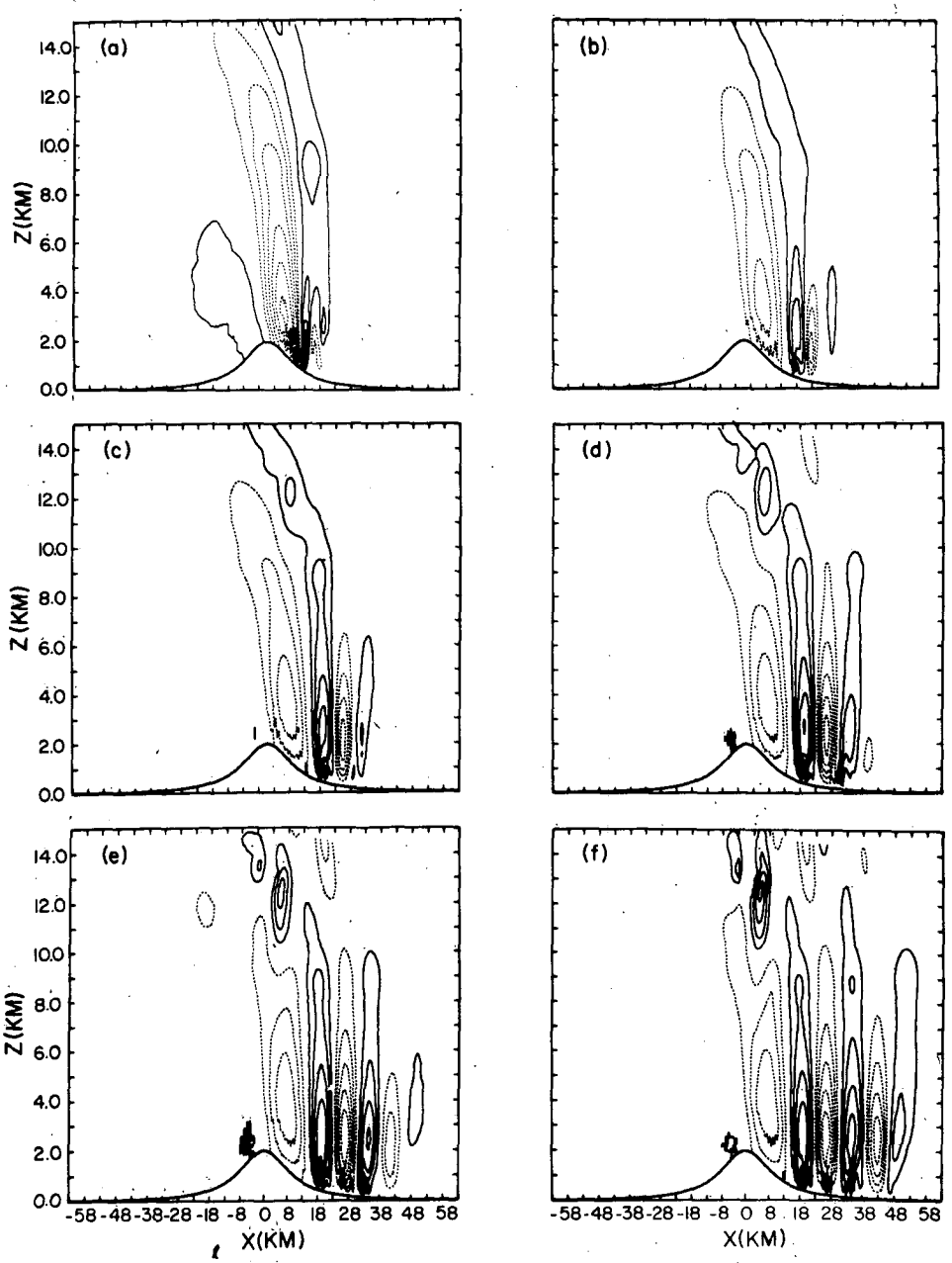

FIG. 23. Evolution of the vertical velocity field for the modified extreme winter model. The times are (a) 1500, (b) 2400, (c) 3150, (d) 3950, (e) 4750 and (f) 5450 s.

1977). It is not at all surprising that this wind storm has been studied in the detail which it has, since it is the only such intense storm for which direct *in situ* measurements of the structure of the wave-field are available. Also available in the above quoted articles are data concerning the height variations of wave momentum flux and turbulence spectra (Lilly, 1978) of the small-scale fluctuations which are associated with the wave itself. In spite of the extent to which this storm has been studied, there has been no fully satisfactory explanation as to why it occurred. We will show in this section that this storm was produced by a nonlinear amplification of the wave which occurred subsequent to its breaking in the lower stratosphere.

The observations which we have to explain are reproduced here for convenience in Figs. 26 and 27 which show, respectively, the observed isentrope field and isopleths of constant horizontal velocity [for a detailed discussion see Lilly (1978)]. To the extent that the dissipation in the wave system may be considered small, the isentropes are equivalent to streamlines. It should be clear by inspection of the θ field for this disturbance that the flow is highly

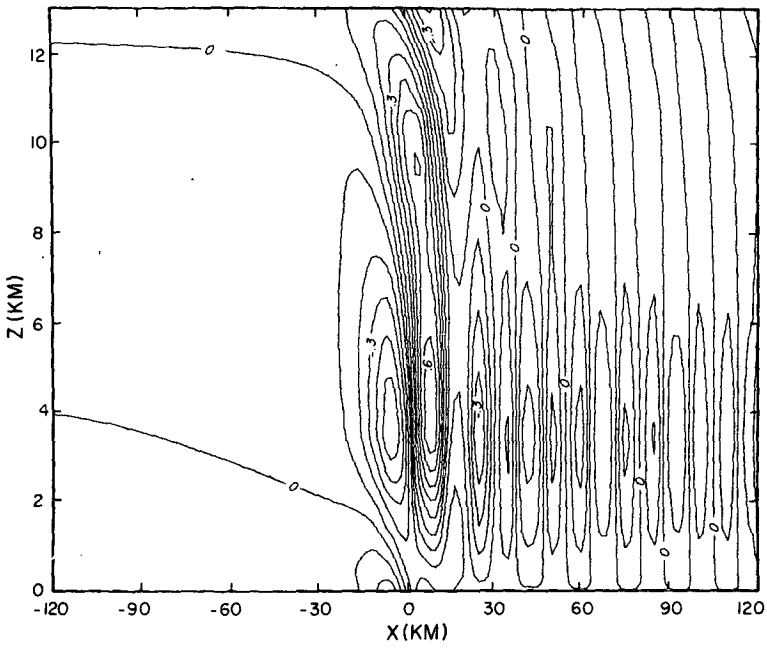

FIG. 24. Steady-state linear vertical velocity pattern for the extreme winter model. This should be compared with Fig. 23f.

nonlinear since the vertical deflection of lines of constant θ is on the order of three times the maximum height of the topography. Also clear in the θ field is the presence of some oscillating streamlines to the lee of the peak in the low levels, indicating that a trapped wave may also be present in the flow. Allowance must of course be made for the fact that the observations on which these figures were based were not simultaneous so that individual small-scale features of the flow should be interpreted with caution.

We must reiterate here the remarks made in I and previously in the present paper regarding the difficulty of describing the evolution of the mountain wave in the strongly nonlinear regime where the wave is breaking using a hydrostatic model which is written in isentropic coordinates. When the wave-induced critical level forms, it is a region in which the vertical gradient of temperature is locally superadiabatic. The transformation to isentropic coordinates is then physically undefined. It seems clear that this must strongly affect the proper simulation of the evolution of the wave in the regime of strong nonlinearity since, as we have shown, strong nonlinearity is synonymous with the occurrence of streamlines which are highly steepened. Since the observed isentropes for the 11 January 1972 wavefield are steepened to the vertical, an

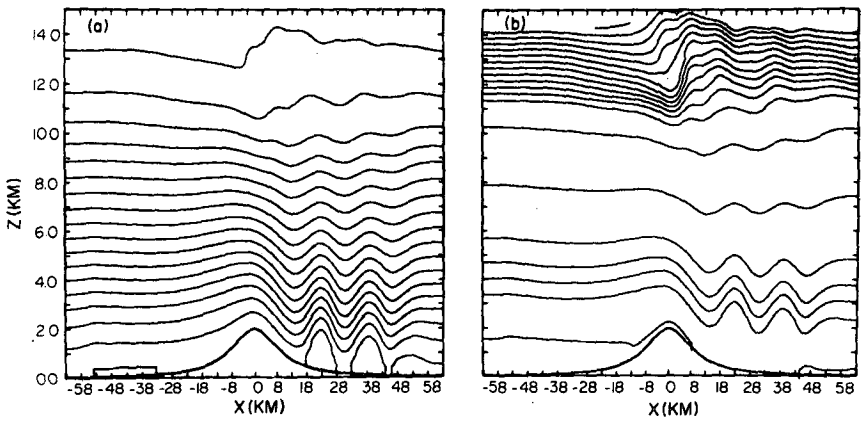

FIG. 25. The streamfunction (a) and isentrope (b) fields for the modified extreme winter case at time t = 5450 s, corresponding to Fig. 23f.

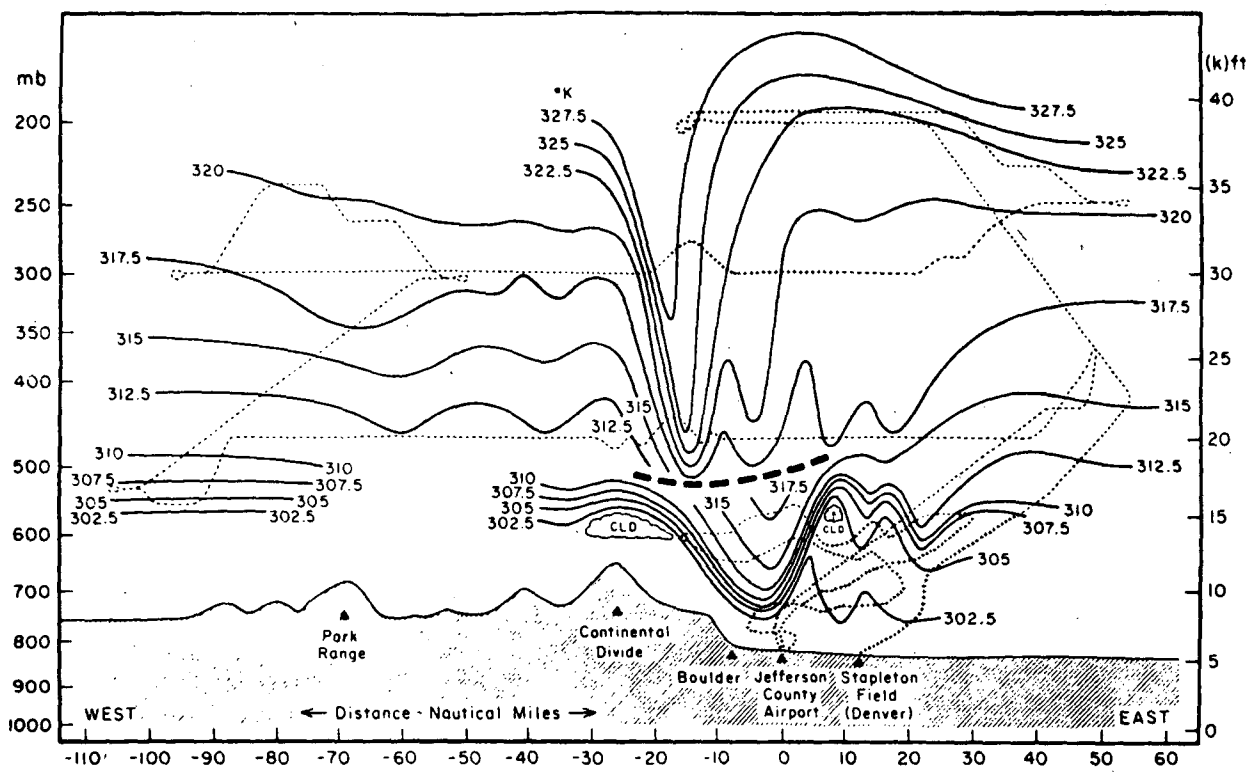

FIG. 26. Isentrope field for the 11 January 1972 severe wind storm in Boulder (after Lilly, 1978).

isentropic coordinate model should not be employed to simulate these observations. The use of a hydrostatic model in the context of this storm may be criticized from a second point of view. In the last section we showed that the upstream profiles were such as to support a rather intense lee wave and that this lee wave completely dominates the linear response. Since such disturbances are intrinsically nonhydrostatic and since they should be present in the response, we suggest that the hydrostatic assumption for the description of the disturbance is invalid *a priori*.

The numerical simulation of the Boulder wind storm data will be described in terms of two separate experiments. For both of the experiments the spatial domain is $N\Delta x \cdot M\Delta z$, where $N = 256$, $M = 84$, $\Delta x = 500$ m and $\Delta z = 341$ m as in the last section. The time step is $\Delta t = 4$ s and the topography is bell-shaped with $a = 10$ km, and $h = 2$ km. The upstream profiles of wind speed and temperature are those shown in Fig. 18 so that the only fundamental difference between the experiments to be described here and those of the last section concerns the stratospheric wind speed which is now 20 m s^{-1} in the accord with the Grand Junction sounding upstream of Boulder on 11 January 1972. The two experiments we shall proceed to describe differ from one another only with respect to the manner in which mixing is treated.

In Fig. 28 we show a series of time slices through the evolving potential temperature field for the first simulation in which a small constant value of K_m is assumed as for the lee wave simulation in the last section. It is clear that a critical level forms just above the tropopause (at $z \approx 11$ km) which is the critical height predicted by linear theory. It is worth repeating, however, that the aspect ratio of the topography is less, by a factor of 2, than the critical aspect ratio predicted by linear theory. This effect, as stated before, is an effect of the nonlinear lower boundary condition. The most important characteristic of the result of this first attempt to simulate the wind storm is clear from the final frames in Fig. 28. As the wave-induced critical level develops, the coherence of the flow in this region degrades rapidly. This is a direct consequence of the fact that the flow in this region has become convectively unstable and the spatial and temporal resolution of the model are insufficient to resolve the secondary "turbulent" motions which ensue. In spite of the loss of coherence, however, the large-scale characteristics of the flow are developing as they must do if the main features of the observed wave field are to be successfully accounted for. Note, in particular, that the tropopause is beginning to fall immediately overhead of the topographic maximum. The calculation suggests that the flow in the lower stratosphere, in the vicinity of

the critical level, should be highly turbulent and this was observed to be the case during the 1972 Boulder wind storm (Lilly, 1978). In order to be able to follow the development of the mountain wave signal further in time, beyond the time of critical-level formation, we must include the diffusive effects of the unresolved turbulent motions which are engendered by physical instability of the resolved scales. In I we employed a first-order closure scheme for this purpose and we return to this approach here.

In Fig. 29 we show a sequence of snapshots of the potential temperature field from the second simulation of the Boulder wind storm. For this calculation the mixing coefficients in the domain interior were calculated on the basis of the first-order closure scheme suggested by Lilly (1962) and previously employed in I. We determined K_m, the mixing coefficient for momentum in (26), from

$$K_m = (k\Delta)^2 |\mathrm{Def}| (1 - \mathrm{Ri})^{1/2} \qquad (44)$$

for $\mathrm{Ri} \lesssim 1$, where Ri is the local value of the gradient Richardson number defined as $\mathrm{Ri} = (gd \ln\theta/dz)/(\mathrm{Def})^2$, where $(\mathrm{Def})^2 = (D_{11}^2 + D_{22}^2)/2 + D_{12}^2$ and D_{ij} is the deformation tensor. In (44) Δ is the grid resolution defined as $\Delta = (\Delta x \cdot \Delta z)^{1/2}$ and k is a numerical constant which is consistent with the Kolmogoroff turbulence spectrum for $k = 0.21$. For the eddy Prandtl number we assumed $\mathrm{Pr} = K_m/K_H = 1$, where K_H is the eddy diffusion coefficient for heat.

The time sequence shown in Fig. 29 begins slightly prior to the end of that shown in Fig. 28 with sufficient overlap to demonstrate the dramatic effect which mixing has near the critical level. Inspection of Fig. 29 shows that subsequent to the breaking of the wave in the lower stratosphere, the magnitude of the downward deflection of the tropopause increases continuously. In the last frame shown this deflection is on the order of 6 km and comparison with the observed field in Fig. 26 reveals a striking similarity. Indeed the differences between theory and observation are sufficiently small that they should be explicable for the most part in terms of differences between the actual and model topography. In Fig. 30 we show the streamfunction corresponding to the last frame in Fig. 29. This picture reveals clearly the consequence of the large deflection of the tropopause. Note that the maximally deflected streamline achieves its maximum deflection just to the lee of the mountain peak and that this streamline enters the upstream boundary of the domain near tropopause height. Since the streamtube bounded above by this streamline and below by the ground has a marked reduction of cross-sectional area to the lee of the peak, it is clear that the wind speed in this region must be extremely high. The unstable

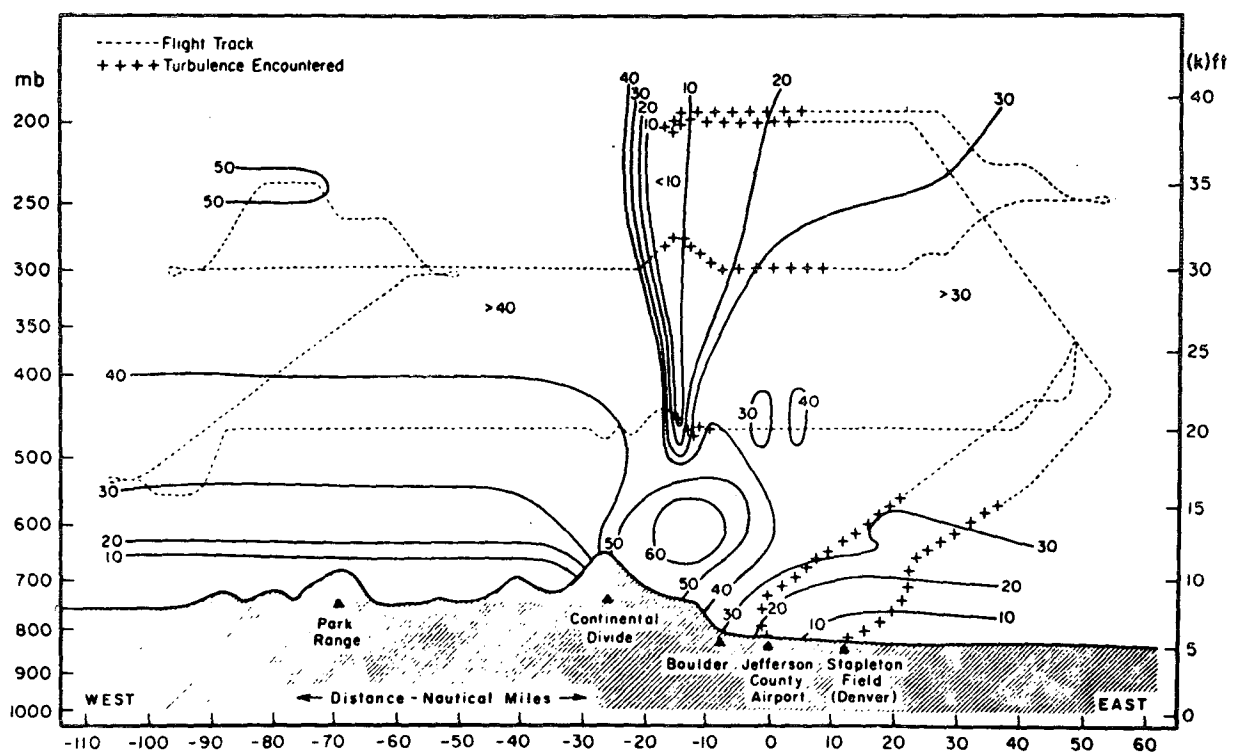

FIG. 27. Horizontal velocity field for the 11 January 1972 severe windstorm in Boulder (after Lilly, 1978).

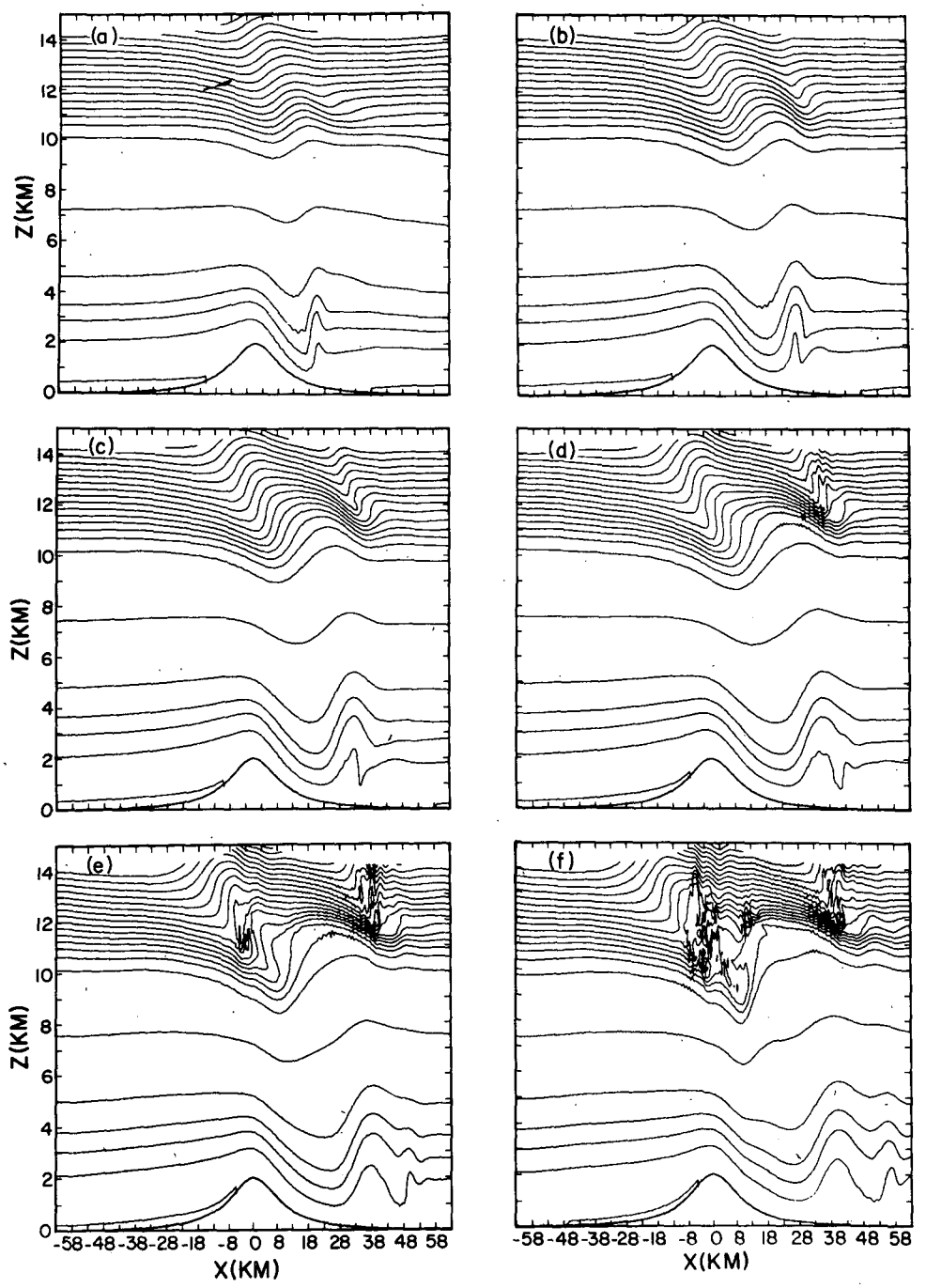

FIG. 28. Isentrope field for first Boulder wind storm simulation with small constant eddy mixing coefficient. Times shown are (a) 1600, (b) 2240, (c) 2880, (d) 3520, (e) 4160 and (f) 4800 s. Note the incoherence of the fields developing in the latest times as the wave breaks.

growth of the wave in the troposphere produces a focusing of the horizontal wind maximum to the lee of the peak.

This effect is clearly revealed in Fig. 31 where we illustrate the evolution in time of the total horizontal velocity field. The time sequence is the same as that in Fig. 29. The last frame in this figure should be compared with the observed field shown in Fig. 27. Again the qualitative and quantitative similarity is striking (the second closed velocity contour to the lee of the peak corresponds to a wind speed of 58 m s^{-1}, which is within a few percent of the observed maximum). In Fig. 32 we show the evolution in time of the surface wave drag for this calcula-

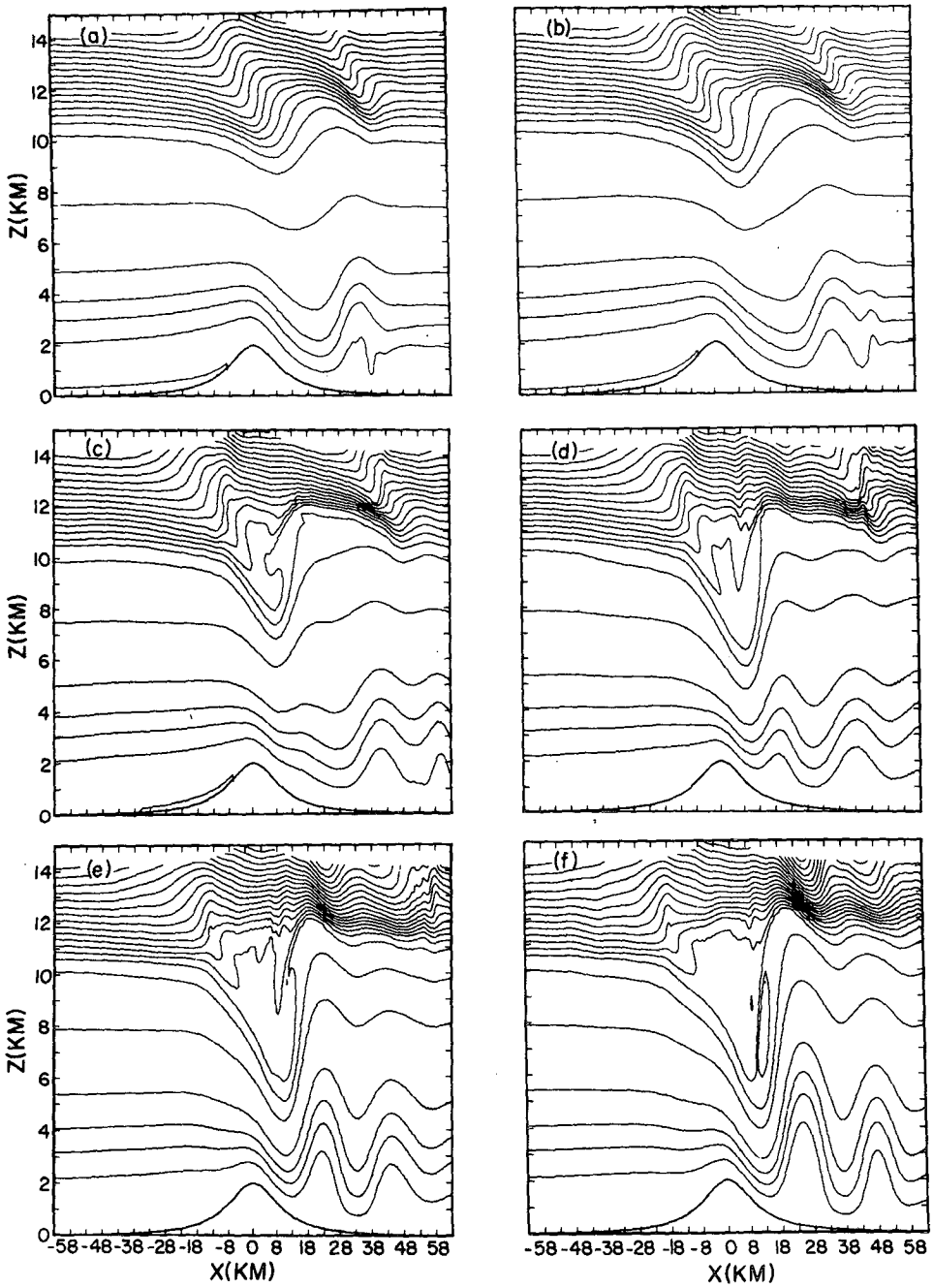

FIG. 29. Isentrope fields for the second Boulder wind storm simulation in which the mixing coefficients are determined through first-order closure. The times shown are (a) 3200, (b) 4160, (c) 5120, (d) 6020, (e) 7040 and (f) 8000 s. Fig. 29b overlaps with Fig. 28e. Note the extreme deflection of the tropopause in the last frame.

tion. The time at which the mountain wave begins to break in the lower stratosphere is marked on the figure. Until this time the flow has a form which is similar to that obtained for the modified mean state discussed in the last section. Subsequent to breaking, the disturbance in the lower troposphere begins to amplify in time and the surface wave drag triples between this time and the time $t = 2000\ \Delta t$ at which we ceased calculation. The final surface drag is in all nearly 20 times higher than the linear prediction.

It seems clear to us that, in order to account for this final and crucial stage of wave amplification which occurs subsequent to breaking in the lower

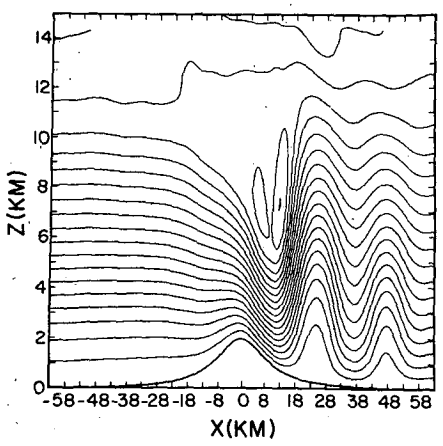

FIG. 30. Streamlines corresponding to the isentrope field in Fig. 29f.

stratosphere, we are obliged to invoke a strong reflection of the mountain wave disturbance from the region of wave breaking and turbulence. After the critical region forms, wave energy which is incident upon it from below is strongly reflected, leading eventually to a sharp decrease in Reynolds stress above the tropopause and a quasi-resonant amplification of the wave between this region and the ground, which is somewhat reminiscent of previous work on the stability of parallel flows (Davis and Peltier, 1976, 1977). The sharp decrease of Reynolds stress above the tropopause is a characteristic feature of the observations (Lilly, 1978) and also of our model simulation of them. We are therefore suggesting that, at least for the 11 January 1972 windstorm, the supercritical steepening and subsequent breaking of the mountain wave in the lower stratosphere played a fundamental dynamical role in the phenomenon. This suggestion is strongly reinforced by the numerical calculations which we have just described.

8. Summary and conclusions

In the preceding sections we have attempted to explore in some detail the range of nonlinear effects which may occur in mountain wave flows. These nonlinear effects may be divided into two classes depending upon whether they may occur only in inhomogeneous flows or whether they also exist when the upstream profiles of wind speed and temperature are constant. In the latter case Long's model applies and appears to explain most of the effects observed in our time-dependent numerical calculations including the sharp increase in wave drag observed when the flow is such that streamlines over the mountain crest are steepened to vertical. Long's model, of course, cannot explain the long time scale which governs the approach to the Long solution in the strongly nonlinear regime. This is almost certainly due to the time dependence of the boundary condition in this regime and should be extractable analytically through application of two timing methods. To our knowledge, this long time scale which appears to govern the approach to the highly nonlinear Long's model states has not been observed previously.

Even for inhomogeneous flows, such as the standard winter model described in Section 5, the dominant nonlinear effects may still be those which would be expected on the basis of Long's model type calculations even though Long's model does not strictly apply to such flows. In the regime of strong nonlinearity where the streamlines are supercritically steepened, the wave drag on the surface is enormously in excess of that which would be predicted on the basis of linear theory. This effect is very important to the phenomenon of strong downslope wind storms since the high-drag states are characterized by a marked increase in the maximum tangential wind speed to the lee of the peak.

Inhomogeneous models may exhibit additional nonlinear phenomena beyond those which are understandable in terms of Long's model when nonhydrostatic effects become sufficiently important. We illustrated the first of these effects in Section 6 by doing a nonlinear calculation for a combination of mean flow and topography for which linear theory predicted the existence of a strong resonant lee wave. The nonlinear calculation not only confirmed the existence of the lee wave in the nonlinear solution but clearly showed that the amplitude of the nonlinear lee wave was very much longer than that predicted by linear theory. It therefore seems that both the hydrostatic and the nonhydrostatic portions of the wave spectrum are enhanced by the nonlinearity when the forcing topography is symmetric. This will almost certainly not be the case for asymmetric topography. That the lee wave amplitude is enhanced by nonlinearity has not been previously demonstrated theoretically although Smith (1976) has commented on the possibility from an observational point of view. The numerical simulation of the nonlinear lee wave in Section 6 is the first, to our knowledge, which has been accomplished with a proper radiation upper boundary condition so that the modes which develop are intrinsic to the stratification and are not simply the normal modes of the box in which the numerical calculation is performed.

In Section 7 we showed that further nonlinear effects due to nonhydrostaticity may occur in inhomogeneous models when the mountain wave

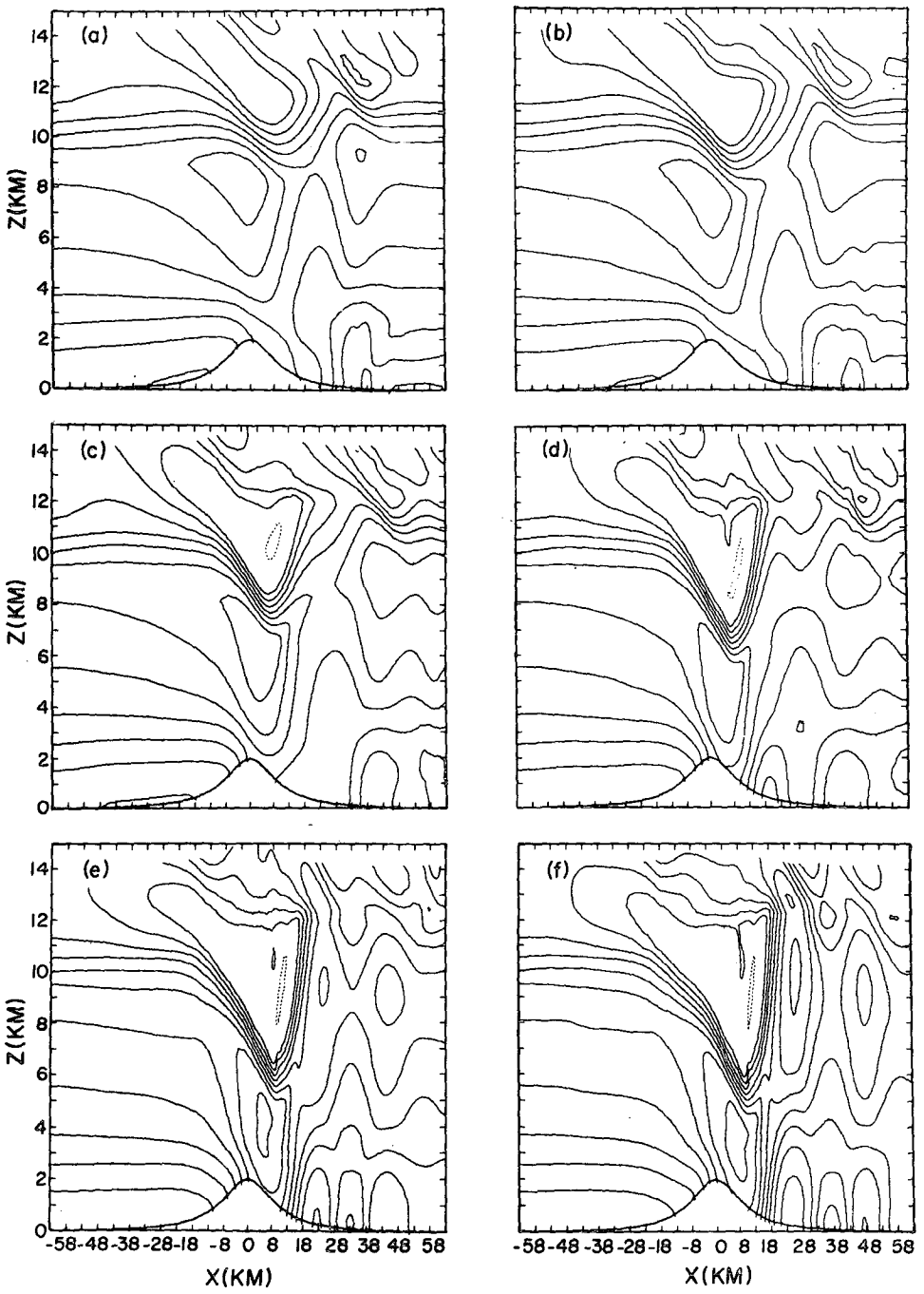

FIG. 31. Total horizontal velocity field for the Boulder wind storm simulation. Times shown are (a) 3200, (b) 4160, (c) 5120, (d) 6020, (e) 7040 and (f) 8000 s. The contour interval is 8 m s^{-1}. In (f) the horizontal wind maximum in the lee of the peak is in excess of 60 m s^{-1}.

actually breaks. Clearly, the convective instability of the wave in the vicinity of the steepening level will be realized only in a nonhydrostatic model where the vertical component of the inertial force may be nonzero. That this instability was realized in our two-dimensional model was shown explicitly by the complete loss of coherence locally as the streamline overturned. When the wave breaks in a realistic atmospheric model and if the point of breaking is located just above the tropopause

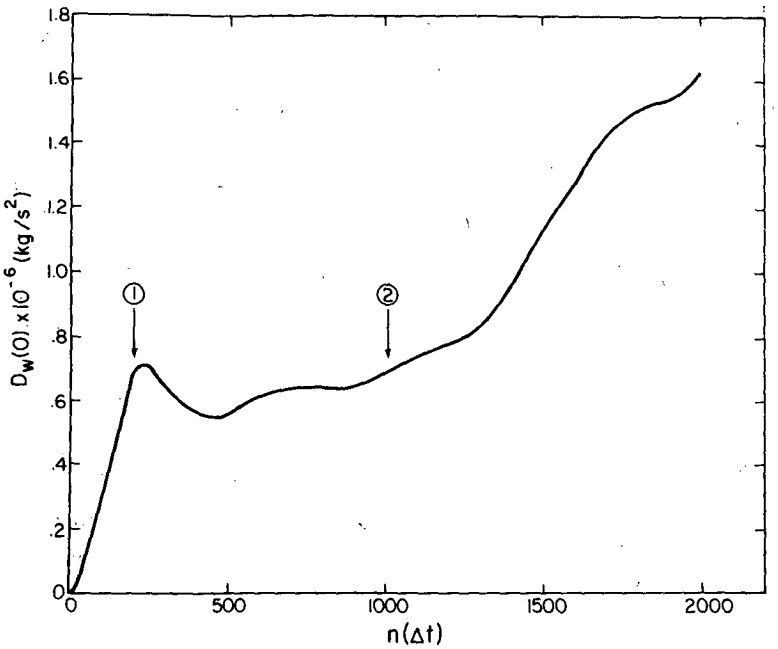

FIG. 32. Surface wave drag as a function of time for the Boulder wind storm simulation. The time step $\Delta t = 4$ s. The time marked 2 is the time at which critical steepening is achieved in the lower stratosphere.

then the mountain wave becomes trapped between the ground and the level of overturning which subsequently acts as a strong reflector of wave energy incident from below. The wave then procedes to amplify in this cavity and the Reynolds stress drops to zero above the point of supercritical steepening. This rather complex process appears to have been responsible for the occurrence of the intense downslope wind storm at Boulder, Colorado, on 11 January 1972 as is well illustrated by our successful numerical simulation of all of the main features of the observed wave field using as input only the upstream soundings of horizontal wind speed and temperature and an admittedly crude approximation to the actual topography. The model appears to have considerable skill as a forecast tool although it would be a rather expensive one!

As mentioned in the Introduction, the existence of such intense nonlinear effects in the mountain wave problem as those which have been documented here raises several important questions concerning the problem of parameterizing the effect of mountain wave drag in atmospheric general circulation models (Lilly, 1972). Current parameterization schemes all make use of the notion of a Reynolds stress drop through a linear critical level (height at which a reversal in mean wind direction occurs). Such calculations of the stress drop have been described by Bretherton (1969). There are two fundamental problems with this idea which are worthy of consideration on the basis of the results discussed here. The first of these concerns the validity of linear theory in estimating the stress drop. As we have shown, the surface wave drag and therefore also the momentum flux in the wave field may be very much greater than linear theory would suggest. Linear theory will therefore provide an underestimate of the deceleration of the mean flow produced by wave absorption at the critical level because it underestimates the momentum flux produced by a given topography. More important, it seems to us, is the fact that linear theory predicts no stress drop unless a linear critical level exists—a fact which follows from the Eliassen-Palm (1960) theorem for stationary waves of sufficiently small amplitude. The work in the present paper shows quite clearly that there may be a large stress drop across the nonlinear wave-induced critical layer. If we employ a linear parameterization scheme to estimate the wave mean flow interaction and thus the contribution of the wave field to the tendency of the resolved synoptic-scale flow, then we will predict no effect under just those conditions when the wave amplitudes and thus the associated momentum transport are largest. It seems clear to us that this must introduce appreciable error.

Acknowledgment. It is a pleasure to acknowledge our indebtedness to M. E. McIntyre, whose careful and critical reading of the first draft of this paper

led us to modify our interpretation of the material in Section 4.

REFERENCES

Blumen, W., 1970: Momentum flux by mountain waves in a stratified rotating atmosphere. *J. Atmos. Sci.*, **22**, 529–534.

——, and C. D. McGregor, 1976: Wave drag by three-dimensional mountain lee waves in non-planar shear flow. *Tellus*, **27**, 287–298.

Bretherton, F. P., 1969: Momentum transport by gravity waves. *Quart. J. Roy. Meteor. Soc.*, **95**, 213–243.

Clark, T. L., 1977: A small scale numerical model using a terrain following coordinate system. *J. Comput. Phys.*, **24**, 186–215.

——, and W. R. Peltier, 1977: On the evolution and stability of finite amplitude mountain waves. *J. Atmos. Sci.*, **34**, 1715–1730.

Davis, P. A., and W. R. Peltier, 1976: Resonant parallel shear instability in the stably stratified planetary boundary layer. *J. Atmos. Sci.*, **33**, 1287–1300.

——, and ——, 1977: Effects of dissipation upon parallel shear instability near the ground. *J. Atmos. Sci.*, **34**, 1868–1884.

Eliassen, A., and E. Palm, 1960: On the transfer of energy in stationary mountain waves. *Geofys. Publ.*, **22**, 1–23.

Gal-Chen, T., and R. C. J. Somerville, 1975: On the use of a co-ordinate transformation for the solution of the Navier-Stokes equations. *J. Comput. Phys.*, **17**, 209–228.

Hines, C. O., and C. A. Reddy, 1967: On the propagation of atmospheric gravity waves through regions of wind shear. *J. Geophys. Res.*, **72**, 1015–1034.

Klemp, J. B., and D. K. Lilly, 1975: The dynamics of wave induced downslope winds. *J. Atmos. Sci.*, **32**, 320–339.

——, and ——, 1978: Numerical simulation of hydrostatic mountain waves. *J. Atmos. Sci.*, **35**, 78–107.

Lester, P. F., 1976: Evidence of long lee waves in southern Alberta. *Atmosphere*, **14**, No. 1, 28–36.

Lilly, D. K., 1962: On the numerical simulation of buoyant convection. *Tellus*, **14**, 145–172.

——, 1972: Wave momentum flux—a GARP problem. *Bull. Amer. Meteor. Soc.*, **53**, 17–23.

——, 1978: A severe downslope windstorm and aircraft turbulence induced by a mountain wave. *J. Atmos. Sci.*, **35**, 59–77.

——, and E. J. Zipser, 1972: The front range windstorm of 11 January 1972—a meteorological narrative. *Weatherwise*, **25**, 56–63.

——, and P. J. Kennedy, 1973: Observations of a stationary mountain wave and its associated momentum flux and energy dissipation. *J. Atmos. Sci.*, **30**, 1135–1152.

Long, R. R., 1972: Finite amplitude disturbances in the flow of inviscid rotating and stratified fluids over obstacles. *Annual Review of Fluid Mechanics*, Vol. 4, Annual Reviews, Inc., 69–92.

McIntyre, M. E., 1972: On Long's hypothesis of no upstream influence in uniformly stratified or rotating flow. *J. Fluid Mech.*, **52**, 209–243.

Miles, J. W., 1969: Waves and wave drag in stratified flows. *Proc. 12th Int. Congress Applied Mechanics*, Hetenyi and Vincenti, Eds., Springer-Verlag, 52–76.

——, and H. E. Huppert, 1969: Lee waves in a stratified flow. Part 4. Perturbation approximations. *J. Fluid Mech.*, **35**, 497–525.

Newell, R. E., J. W. Kidson, D. G. Vincent and G. J. Boer, 1972: *The General Circulation of the Tropical Atmosphere and Interactions With Extra-Tropical Latitudes*. The MIT Press, 258 pp.

Orlanski, I., 1976: A simple boundary condition for unbounded hyperbolic flows. *J. Comput. Phys.*, **21**, 251.

Smagorinski, J., 1963: General circulation experiments with the primitive equations: I. The basic experiment. *Mon. Wea. Rev.*, **91**, 99–164.

Smith, R. B., 1976: The generation of lee waves by the Blue Ridge. *J. Atmos. Sci.*, **33**, 507–519.

——, 1977: The steepening of hydrostatic mountain waves. *J. Atmos. Sci.*, **34**, 1634–1654.

Vergeiner, I., 1971: An operational linear lee wave model for arbitrary basic flow and two dimensional topography. *Quart. J. Roy. Meteor. Soc.*, **97**, 30–56.